

## Article

# Sustainable Napier Grass (*Pennisetum purpureum*) Biochar for the Sorptive Removal of Acid Orange 7 (AO7) from Water

Anand Kumar Yadav , Abhishek Kumar Chaubey , Shivang Kapoor, Tej Pratap, Brahmacharimayum Preetiva, Vineet Vimal and Dinesh Mohan \* 

School of Environmental Sciences, Jawaharlal Nehru University, New Delhi 110067, India; anand12\_ses@jnu.ac.in (A.K.Y.); abhish94\_ses@jnu.ac.in (A.K.C.); shivan47\_ses@jnu.ac.in (S.K.); tej94\_ses@jnu.ac.in (T.P.); brahma76\_ses@jnu.ac.in (B.P.); vineet18\_ses@jnu.ac.in (V.V.)

\* Correspondence: dm\_1967@hotmail.com

**Abstract:** The unregulated discharge of synthetic dyes from various anthropogenic and industrial activities has resulted in the contamination of different environmental compartments. These dyes can contaminate water bodies, soil, and even the air, resulting in many environmental and health issues. True colors may persist for long periods, thereby affecting the aesthetics and ecology of dye-contaminated areas. Furthermore, they pose potential risks to aquatic life and human health through the ingestion or absorption of dye-contaminated water or food. Acid orange 7 (AO7) is a synthetic azo dye used in the textile, tanning, food, pharmaceutical, paint, electronics, cosmetics, and paper and pulp industries. AO7 can have various human health implications, such as dermatitis, nausea, severe headache, respiratory tract irritation, and bone marrow depletion, due to its high toxicity, mutagenicity, and carcinogenicity. Efforts to regulate and mitigate dye pollution (AO7) are crucial for environmental sustainability and public health. Therefore, this study aimed to remove AO7 from water using sustainable biochar. This objective was accomplished by pyrolyzing dried Napier grass at 700 °C to develop affordable and sustainable Napier grass biochar (NGBC700). The developed biochar was characterized for its surface morphology, surface functional groups, surface area, and elemental composition. The yield, moisture content, and ash content of the NGBC700 were approximately 31%, 6%, and 21%, respectively. The NGBC700's BET (Brunauer–Emmett–Teller) surface area was 108 m<sup>2</sup> g<sup>−1</sup>. Batch sorption studies were carried out at different pH levels (2–10), biochar dosages (1, 2, 3, and 4 g L<sup>−1</sup>), and AO7 concentrations (10, 20, and 30 mg L<sup>−1</sup>). The kinetic data were better fitted to the pseudo-second-order (PSO) equation ( $R^2 = 0.964–0.997$ ) than the pseudo-first-order (PFO) equation ( $R^2 = 0.789–0.988$ ). The Freundlich isotherm equation ( $R^2 = 0.965–0.994$ ) fitted the sorption equilibrium data better than the Langmuir equation ( $R^2 = 0.788–0.987$ ), suggesting AO7 sorption on heterogeneous NGBC700. The maximum monolayer AO7 adsorption capacities of the NGBC700 were 14.3, 12.7, and 8.4 mg g<sup>−1</sup> at 10, 25, and 40 °C, respectively. The column AO7 sorption capacity was 4.4 mg g<sup>−1</sup>. Fixed-bed AO7 sorption data were fitted to the Thomas and Yoon–Nelson column models. The NGBC700 efficiently removed AO7 from locally available dye-laden wastewater. NGBC700 was regenerated using different NaOH concentrations. Possible interactions contributing to AO7 sorption on NGBC700 include hydrogen bonding, electrostatic interactions, and  $\pi$ – $\pi$  electron donor–acceptor attractions. The estimated total preparation cost of NGBC700 was US\$ 6.02 kg<sup>−1</sup>. The developed sustainable NGBC700 is potentially cost-effective and environmentally friendly, and it utilizes waste (Napier grass) to eliminate fatal AO7 dye from aqueous media.

**Keywords:** elephant grass; lignocellulosic waste; pyrolysis; biochar; batch sorption; fixed-bed study; acid orange 7 (AO7)



**Citation:** Yadav, A.K.; Chaubey, A.K.; Kapoor, S.; Pratap, T.; Preetiva, B.; Vimal, V.; Mohan, D. Sustainable Napier Grass (*Pennisetum purpureum*) Biochar for the Sorptive Removal of Acid Orange 7 (AO7) from Water. *Processes* **2024**, *12*, 1115. <https://doi.org/10.3390/pr12061115>

Academic Editor: Antoni Sánchez

Received: 4 May 2024

Revised: 19 May 2024

Accepted: 22 May 2024

Published: 28 May 2024



**Copyright:** © 2024 by the authors. Licensee MDPI, Basel, Switzerland. This article is an open access article distributed under the terms and conditions of the Creative Commons Attribution (CC BY) license (<https://creativecommons.org/licenses/by/4.0/>).

## 1. Introduction

Synthetic dyes in water systems pose a severe environmental threat due to their persistence, mutagenicity, carcinogenicity and toxicity. They subsequently harm aquatic

ecosystems and human well-being [1,2]. High concentrations of dyes obstruct sunlight transmission in receiving water systems and radically reduce their reoxygenation capacities, disrupting the photosynthesis and respiration of aquatic flora and fauna [3]. A dye concentration of even less than  $1 \text{ mg L}^{-1}$  in water is visible and undesirable, marking the dye as an “aesthetically unacceptable contaminant” [4]. Fish inhabiting dye-contaminated water bioaccumulate dyes, which accumulate through the food chain and eventually reach human beings [5]. Dye toxicity may lead to dysfunction of the reproductive system, kidneys, liver, brain, and central nervous system [6]. Even the degradation products of dyes are highly toxic, carcinogenic, and mutagenic [7].

Dye-containing wastewater from various industries including the textile, paint, paper and pulp, cosmetics, plastic, chemical, pharmaceutical, and tanning industries is usually discharged into natural streams after inadequate treatment. The textile industry is a grossly polluting industry that generates a very high volume of dye-containing wastewater which is characterized by a high biological oxygen demand (BOD), chemical oxygen demand (COD), pH, pollutant load, total dissolved solids (TDS) content, and suspended solids content [8,9]. The Indian textile industry alone consumes ~830 billion L/year of water and discharges ~640 billion L/year of dye-containing wastewater [10]. A global annual loss of ~280,000 tons of unfixed dyes into effluents has been reported due to inefficient dyeing processes within the textile industry [11]. More than 50% of these unfixed dyes are azo dyes [12]. They are identified by a functional group ( $-\text{N}=\text{N}-$ ) that links two identical or different alkyl or aryl radicals which can be symmetrical, asymmetrical, or non-azo [13]. They act as colorants and contain chemical groups that can establish covalent bonds with textile substrates [14]. Acid orange 7 (AO7) is an acidic azo dye frequently used to dye silk, wool, paper products, leather, and washing agents. [15]. Other commercial applications of AO7 include its use as a wood preservative, food dye, hair dye, ink, and acid–base indicator [16]. Long-term exposure to AO7 can cause nausea, severe headache, bone marrow depletion, and irritation of the skin, eye, mucous membranes, and respiratory tract [17,18]. The degradation products of AO7, including 2-naphthol, 1,4-benzoquinone, and 1-amino-2-naphthol, are considered more toxic than the parent compound [19]. Aromatic amine (1-amino-2-naphthol), one of the reductive degradation products of AO7, is a highly water-soluble, toxic, and carcinogenic compound which can induce cell mutation, methemoglobinemia, and bladder tumors [20]. AO7 is a significant water contaminant/pollutant due to its sizeable commercial production (due to its various commercial applications) and indiscriminate discharge into water bodies without proper treatment.

Advanced oxidation processes [21–23], electrochemical oxidation [24,25], membrane filtration [26,27], coagulation–flocculation [28], biological treatment [29], and adsorption [30,31] have been explored for AO7 removal. Adsorption is preferred for dye removal over other methods because of its simpler design, ease of handling, excellent removal efficiency, economic feasibility, and absence of secondary contamination [32]. Batch, semicontinuous, and continuous sorption modes are available in adsorption systems [33]. Activated carbons [34–36], metal–organic frameworks [37], red mud and clay [38], biosorbents [39,40], fly ash [41], nanoparticles [42,43], chitosan [44], industrial by-products [45], polymers [46], and biochar [47–49] have been used for AO7 removal. AO7 has been removed from water using biochar/modified biochar prepared from 40% phosphoric acid-treated lemon peel (pyrolyzed at  $500^\circ\text{C}$  for 1 h) [47], red mud with shaddock peel (pyrolyzed at  $300\text{--}800^\circ\text{C}$  for 2 h with a  $10^\circ\text{C min}^{-1}$  heating rate) [48], and *Cucumis sativus* peel (pyrolyzed at  $500^\circ\text{C}$  with a  $10^\circ\text{C min}^{-1}$  ramp rate for 3 h) [49]. Biochar is a low-cost alternative to commercially available activated carbon, nanomaterial, and MOFs [50]. It is a carbonaceous solid obtained from the pyrolysis of lignocellulosic waste/biomass in an oxygen-limited environment [51]. Biochar can be prepared from feedstocks including agricultural waste, forestry waste, food waste, municipal waste, and invasive plants. This also provides solutions to environmental problems related to solid waste management. Biochar is preferred over other adsorbents due to its low cost, sustainability, high porosity, good sorption capacity,

fast kinetics, moderate to high surface area, and ease of regeneration [52–54]. Typically, the sorption of organic compounds tends to increase as the pyrolysis temperature of biochar rises [50]. Therefore, in this study, biochar was prepared at a high temperature (700 °C) to treat AO7. Napier grass, also known as elephant grass or Uganda grass, is an invasive grass species which can compete with and outgrow the natural vegetation in any region, even under water stress conditions, thus harming the biodiversity of the region [55–57]. It has a yearly production capacity of ~45 T of dry material/ha [56]. Given its rapid growth, low disease risk, and capacity to flourish in a variety of soil types, even with lower inputs of nitrogen fertilizer, it may be a promising source of biochar feedstock [56–58]. With 30 tons per hectare of production, it may produce ~1.2 GT of charcoal and 2 GT of bio-oils annually [56,59]. Thus, it was chosen as a precursor for biochar production.

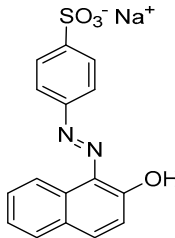
The present study offers a solid foundation for further research into the application of Napier grass biochar (NGBC700) by utilizing it as an adsorbent to remediate AO7-dye-contaminated water. The Napier grass biochar was used without any additional physical or chemical treatment at a near-neutral pH (~6.5). This study was performed in both batch and column modes. The effects of pH, initial dye concentration, adsorbent dose, and temperature were studied for AO7 sorption on NGBC700. Possible AO7 sorption interactions on NGBC700 were also established. The NGBC700 preparation cost was estimated using a simple analysis and compared with commercial activated carbon to justify its economic feasibility. To prevent any pollution that may arise from the activities of local dyers, the NGBC700 was used to remediate AO7 from locally available dye-laden wastewater. Further, continuous AO7 sorption onto NGBC700 was carried out in a downflow fixed-bed adsorber, and the obtained data were fitted to Thomas and Yoon–Nelson fixed-bed models. These column parameters will be helpful in establishing large treatment plants for treating textile wastewater rich in AO7 using NGBC700. Finally, the NGBC700 was regenerated and reused for three adsorption–desorption cycles.

## 2. Materials and Methods

### 2.1. Reagents and Apparatus

AO7 (AR, molar mass = 350.32 g mol<sup>−1</sup>), hydrochloric acid (HCl), and sodium hydroxide (NaOH) were procured from Sigma-Aldrich chemical pvt. limited, India. Sodium chloride (NaCl) was purchased from Qualigens, India. HCl and NaOH were used to maintain the pH of solutions, and NaCl was utilized to determine the pH at point zero charge (pH<sub>pzc</sub>). The wavelength at maximum absorbance (λ<sub>max</sub>) for AO7, i.e., 485 nm, was chosen using UV–visible spectrophotometry (PerkinElmer, Shelton, CT, USA). The chemical structure and properties of AO7 are mentioned in Table 1.

**Table 1.** Chemical structure and properties of acid orange 7.

Properties	Acid Orange 7 (AO7)
Chemical structure	
Empirical formula	C <sub>16</sub> H <sub>11</sub> N <sub>2</sub> NaO <sub>4</sub> S
Solubility (in water)	116 g L <sup>−1</sup> at 30 °C
IUPAC name	Sodium 4-[(2E)-2-(2-oxonaphthalen-1-ylidene)hydrazinyl]benzenesulfonate
Molar mass	350.32 g mol <sup>−1</sup>
CAS No.	633-96-5
Generic name	Acid orange 7 (C. I. 15510)
Class	Azo dye (anionic)

## 2.2. Development of NGBC700

Napier grass was collected from a farm in Mohammad Pur near the bank of the Yamuna River, Delhi (28°48'17.2" N 77°11'12.0" E), India. It was cleaned and sun-dried. The sun-dried Napier grass was cut into pieces and oven-dried at 80 °C for 8 h (Figure 1). The dried Napier grass was pyrolyzed for 1 h at 700 °C (heating rate = 10 °C min<sup>-1</sup>) in a muffle furnace. The biochar produced was ground and sieved to a particle size of 52–100 B.S.S. mesh (300–150 µm). The sieved biochar was washed several times with distilled water to remove soluble organics and ash until no wash-water absorbance peak was observed in the visible spectrum range. The biochar was then oven-dried at 90 °C for 8 h; afterwards, it was packed in an airtight container and labeled NGBC700.

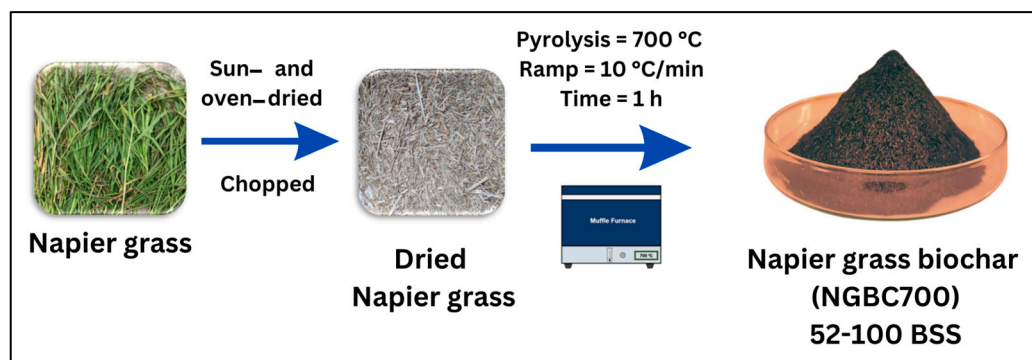


**Figure 1.** Preparation of Napier grass biochar (NGBC700).

## 2.3. Characterization of NGBC700

The biochar yield (%) was estimated using Equation (1). The  $\text{pH}_{\text{pzc}}$  of the NGBC700 was determined by the method described earlier, using a Thermo-Scientific Orion 5 Star (Beverly, MA, USA) pH meter [60]. The ash content of the biochar was estimated using the ASTM-D1762-84 thermogravimetric method [61]. The NGBC700's metal contents were determined through the wet digestion method by dissolving ash into aqua regia using ICP-OES (Agilent 5100, Mulgrave, Victoria, Australia). The biochar's total percentages of C, H, N, and S contents were determined using an Elementar Vario EL Cube CHNS analyzer (Langenselbold, Germany). The oxygen (%) content was estimated by subtracting the (%) contents of the above elements from 100%, as shown in Equation (2). The elemental composition of the NGBC700's surface was estimated (down to a 2 µm depth) using an EDX analysis. A Bruker EDX system (Berlin, Germany) equipped with a Zeiss EVO40 SEM system (Cambridge, United Kingdom) was used to perform an energy-dispersive X-ray analysis. Different characteristics of the biochar, such as its surface morphology, surface area, pore structure, surface functional groups, total pore volume, and pore radius, were determined using various instruments, as mentioned in Table S1.

$$\text{Biochar yield (\%)} = \frac{\text{Mass of biochar (M}_{\text{bc}})}{\text{Mass of biomass (M}_{\text{bm}})} \times 100 \quad (1)$$

$$\text{O (\%)} = 100 (\%) - \text{C (\%)} - \text{H (\%)} - \text{N (\%)} - \text{S (\%)} - \text{Ash (\%)} \quad (2)$$

## 2.4. Batch Sorption Studies

An acid orange 7 stock solution (1000 mg L<sup>-1</sup>) was prepared using double-distilled water (DDW). This stock solution was used to prepare fresh AO7 solutions for batch and column sorption experiments. The effect of pH on the sorption of AO7 onto NGBC700 was examined at pH values of 2, 4, 6, 8, and 10 (NGBC700 dose: 2 g L<sup>-1</sup>; AO7: 10 mg L<sup>-1</sup>; temp.: 25 °C). The adsorbate/adsorbent suspensions were taken in a container and properly mixed using a water bath incubator shaker at 25 °C for 24 h. A pH of 6.5 and an agitation speed of 100 rpm were chosen for all sorption studies. The sorption experiments were performed in duplicates, and mean values along with standard deviations are reported.



The AO7 percent removal and sorption capacity ( $\text{mg g}^{-1}$ ) on NGBC700 were calculated using Equations (3) and (4), respectively.

$$\text{Removal (\%)} = \frac{(C_0 - C_e)}{C_0} \times 100 \quad (3)$$

$$\text{Sorption capacity (q}_e\text{)} = \frac{(C_0 - C_e)V}{M} \quad (4)$$

where  $C_0$  ( $\text{mg L}^{-1}$ ) is the initial AO7 concentration and  $C_e$  ( $\text{mg L}^{-1}$ ) is the equilibrium AO7 concentration.  $V$  (L) is the AO7 solution volume, and  $M$  (g) is the mass of biochar used in the experiment.

Sorption kinetics were determined at different biochar doses (1, 2, 3, and 4  $\text{g L}^{-1}$ ) and AO7 concentrations (10, 20, and 30  $\text{mg L}^{-1}$ ) for time intervals [(5 min, 15 min, 30 min, 45 min, 1 h, 2 h, 4 h, 6 h, 8 h, 16 h, 24 h, and 48 h)] at 25 °C.

Non-linear pseudo-first-order (PFO) [62] and pseudo-second-order (PSO) [63] kinetic equations were applied to the sorption kinetic data, as shown in Equations (5) and (6), respectively.

$$q_t = q_e(1 - e^{-k_1 t}) \quad (5)$$

$$q_t = \frac{q_e^2 k_2 t}{1 + q_t k_2 t} \quad (6)$$

where  $k_1$  ( $\text{h}^{-1}$ ) and  $k_2$  ( $\text{g mg}^{-1} \text{h}^{-1}$ ) are the PFO and PSO kinetic equations' rate constants, respectively.  $q_e$  and  $q_t$  ( $\text{mg g}^{-1}$ ) are the adsorption capacities at equilibrium and at time  $t$  (h), respectively.

Sorption isotherm studies were conducted in a 10–250  $\text{mg L}^{-1}$  AO7 concentration range at 10, 25, and 40 °C. The AO7 solution pH, NGBC700 particle size, and dose for the isotherm study were 6.5, 52–100 BSS, and 2  $\text{g L}^{-1}$ , respectively. Non-linear Langmuir (Equation (7)) and Freundlich (Equation (8)) isotherm models were fitted on the sorption equilibrium data. The adsorption of molecules on a perfectly uniform surface is suitable for the Langmuir isotherm model, which implies a single layer of coverage of the adsorbate on the adsorbent [64]. On the other hand, the Freundlich isotherm is more versatile and can be applied to situations in which adsorption occurs on heterogeneous surfaces and involves multilayer sorption [65].

$$q_e = \frac{Q^\circ b C_e}{1 + b C_e} \quad (7)$$

$$q_e = K_F C_e^{\frac{1}{n}} \quad (8)$$

where  $q_e$  and  $Q^\circ$  are the equilibrium and monolayer adsorption capacity ( $\text{mg g}^{-1}$ ),  $b$  ( $\text{L mg}^{-1}$ ) is the Langmuir equilibrium constant,  $C_e$  ( $\text{mg L}^{-1}$ ) is the equilibrium AO7 concentration,  $K_F$  ( $\text{mg g}^{-1}$ ) is the Freundlich sorption constant,  $n$  is the Freundlich exponent, and  $1/n$  is a measure of the adsorption intensity.

## 2.5. NGBC700 Regeneration

It is very important to select an appropriate eluent for desorption and regeneration of an adsorbent [66]. AO7 desorption was initially carried out with 0.1 N NaOH, 0.1 N HCl, 0.1 N NaCl and 10% EtOH. Based on the preliminary studies, NaOH was finally selected for dye desorption studies. Moreover, desorption of adsorbed AO7 on NGBC700 was performed using NaOH solutions of varying concentrations: 0.01, 0.05, 0.1, 0.5, and 1 N. In summary, 0.1 g of NGBC700 was added to 50 mL of an aqueous AO7 solution (conc. = 20  $\text{mg L}^{-1}$ ; pH = 6.5). The mixture was then agitated at 100 rpm in a water bath incubator shaker at 25 °C for 24 h. Then, the spent NGBC700 was filtered and kept in the oven to dry for 6 h at 95 °C. The dried NGBC700 was cooled and then agitated with 50 mL

of a desorbing agent for 24 h, filtered, and washed with DDW. The filtered NGBC700 was oven-dried for 6 h at 95 °C and left to cool at room temperature. Adsorption-desorption studies were carried out for up to three cycles to assess its reusability potential. The AO7 concentration was quantified after each sorption cycle via UV–vis spectroscopy.

## 2.6. Column Study

In industrial applications involving the removal of contaminants, fixed-bed studies are crucial and necessary [33,67,68]. It is simple to apply design parameters from fixed-bed-column studies to large-scale commercial applications [33,67,68]. A schematic representation and actual picture of the column setup, along with the ideal breakthrough curve, are given in Figure S1. A fixed-bed study was performed by utilizing a 45 cm long glass column (2 cm internal dia.). As a column support, glass wool was used to run the fixed-bed column in the downflow mode under gravity [67,68]. A slurry comprising 4 g of Napier grass biochar (NGBC700) was prepared using lukewarm double-distilled water (DDW). An NGBC700 fixed bed (bed depth = 11 cm) was formed by adding the biochar slurry to a glass wool-supported fixed-bed column. Initially, 20 mg L<sup>−1</sup> of AO7 at a pH of 6.5 was introduced into the column at room temperature (~27 °C). The eluent was collected at fixed time intervals, and the AO7 was measured using a UV–visible spectrophotometer at a λ<sub>max</sub> of 485 nm [35,36].

A breakthrough curve analysis was used to assess the dynamic behavior of the fixed-bed column [33,67,69]. Breakthrough curves for the fixed-bed study under the given experimental conditions were generated by plotting C<sub>t</sub>/C<sub>0</sub> against time [33,67,69]. Here, C<sub>t</sub> represents the adsorbate concentration in the effluent and C<sub>0</sub> represents the adsorbate concentration in the initial inlet. In this study, breakthrough and exhaustion were considered to occur at C<sub>t</sub>/C<sub>0</sub> values of 0.1 and 0.9, respectively.

The column's performance was monitored using a breakthrough curve, employing Weber's mass transfer model [33,67]. Several fixed-bed sorption parameters were calculated using Equations (9)–(14).

$$t_x = \frac{V_x}{F_m} \quad (9)$$

$$t_\delta = \frac{V_x - V_b}{F_m} \quad (10)$$

$$f = 1 - \frac{t_f}{t_\delta} \quad (11)$$

$$\% \text{ Saturation} = \frac{D - \delta(f)}{D} \times 100 \quad (12)$$

$$\text{EBCT} = \frac{\text{Bed Volume (mL)}}{\text{flow rate} \left( \frac{\text{mL}}{\text{min}} \right)} \quad (13)$$

$$\text{Adsorbent usage rate} \left( \frac{\text{g}}{\text{L}} \right) = \frac{\text{Weight of adsorbent in column (g)}}{\text{Volume of effluent at breakthrough (L)}} \quad (14)$$

Further, the column's adsorption capacity was determined using total area under the breakthrough curve (A<sub>c</sub>) (Figure S1) obtained for AO7 sorption on NGBC700 [70,71]. Therefore, calculating the integral area under the breakthrough curve between C<sub>ads</sub> (C<sub>0</sub>–C<sub>t</sub>) and time (t) yielded the quantity of AO7 adsorbed (Equation (15)).

$$A_c = \int_{t=0}^{t=t_{\text{total}}} C_{\text{ads}} dt \quad (15)$$

By replacing A<sub>c</sub> in Equation (16), the overall adsorbed AO7 (Q<sub>total</sub>) can be computed.

$$Q_{\text{total}} = \frac{QA_c}{1000} = \frac{Q}{1000} \int_{t=0}^{t=t_{\text{total}}} (C_0 - C_t) * dt \quad (16)$$

where  $Q$  denotes the total inflow rate represented in “ $\text{mL min}^{-1}$ ”.

The maximum AO7 column adsorption capacity was determined using the Equation (17).

$$q_{\text{exp}} \left( \frac{\text{mg}}{\text{g}} \right) = \frac{Q_{\text{total}}}{m} \quad (17)$$

where  $m$  (g) represents the quantity of NGBC700 utilized within the column.

### 2.6.1. Thomas Model

The Thomas model is widely used fixed-bed sorption model. This model is based on the pseudo-second-order kinetic and Langmuir isotherm equations [33,69,72]. Equation (18) represents the linear form of the Thomas model [33,69,73].

$$\ln \left[ \left( \frac{C_0}{C_t} \right) - 1 \right] = \left( \frac{K_{\text{TH}} \cdot q_{\text{max}} \cdot m}{Q} \right) - K_{\text{TH}} C_0 t \quad (18)$$

where  $C_t$  ( $\text{mg L}^{-1}$ ) represents the effluent concentration at time  $t$ ,  $C_0$  stands for the initial influent concentration,  $t$  (min) denotes the sampling time,  $K_{\text{TH}}$  ( $\text{mL min}^{-1} \text{mg}^{-1}$ ) signifies the Thomas rate constant,  $m$  (g) indicates the amount of NGBC700 in the column,  $q_{\text{max}}$  ( $\text{mg g}^{-1}$ ) represents the maximum adsorbate concentration in the solid phase, and  $Q$  ( $\text{mL min}^{-1}$ ) denotes the influent flow rate. Additionally,  $q_{\text{max}}$  and  $K_{\text{TH}}$  were determined from the intercept  $\left( \frac{K_{\text{TH}} \cdot q_{\text{max}} \cdot m}{Q} \right)$  and slope ( $K_{\text{TH}} \cdot q_{\text{max}}$ ) of the linear plot between  $\ln \left[ \left( \frac{C_0}{C_t} - 1 \right) \right]$  and “ $t$ ” [33,69].

### 2.6.2. Yoon–Nelson Model

The Yoon–Nelson model is a simple fixed-bed adsorption model [69,74]. The linear form of the Yoon–Nelson model is expressed in Equation (19) [33,69].

$$\ln \left[ \left( \frac{C_t}{C_0 - C_t} \right) - 1 \right] = K_{\text{YN}}(t - \tau) \quad (19)$$

where  $C_0$  ( $\text{mg L}^{-1}$ ) represents the influent AO7 conc., and  $C_t$  ( $\text{mg L}^{-1}$ ) signifies the effluent concentration at a specific time.  $K_{\text{YN}}$  denotes the rate constant ( $\text{min}^{-1}$ ),  $\tau$  is the time required for 50% adsorbate breakthrough to occur (min), and  $t$  represents the time of breakthrough (min).  $K_{\text{YN}}$  and  $\tau$  were determined using the slope and intercept obtained by plotting the natural logarithm of  $(C_t/C_0 - C_t)$  against time [33,69].

### 2.7. NGBC700 Preparation Cost

In order to treat water/wastewater on a commercial scale, estimating the adsorbent preparation cost is essential [68,75,76]. In low- and middle-income nations, the absorbent cost becomes particularly crucial for widespread acceptability [68]. The NGBC700 cost analysis considered several steps, such as Napier grass collection and transportation, size reduction, pyrolysis, subsequent biochar size reduction, washing, and the final oven-drying process. Possible cost estimation was performed using a modified methodology previously developed and employed by other researchers (Equation (20)) [68,75,76].

$$\text{COST}_{\text{BC}} = \text{COST}_{\text{P}} + \text{COST}_{\text{Pro}} + \text{COST}_{\text{A/M}} + \text{COST}_{\text{Py}} + \text{COST}_{\text{OTHER}} \quad (20)$$

where  $\text{COST}_{\text{BC}}$  is the total cost of preparing the NGBC700,  $\text{COST}_{\text{P}}$  is the precursor procurement cost,  $\text{COST}_{\text{Pro}}$  is the precursor processing cost (including size reduction and drying),  $\text{COST}_{\text{A/M}}$  is the precursor activation or modification cost,  $\text{COST}_{\text{Py}}$  is the pyrolysis and post-processing cost (comprising electricity, washing, and drying costs), and  $\text{COST}_{\text{OTHER}}$  includes miscellaneous costs and a 10% offset for any biochar loss experienced during the entire process. In this study,  $\text{COST}_{\text{A/M}}$  remained zero since there were no activation/modification steps involved in preparing the NGBC700. All costs were calculated

in Indian rupees (IN₹) and then converted to US dollars (US\$) using the exchange rate of 1 US\$ = IN₹ 83.11 as of 13 May 2024. Finally, the total cost was calculated and reported in US dollars (US\$) and Indian Rupees (IN₹) per kg of NGBC700.

### 2.8. NGBC700 Application in Actual Dye Wastewater Treatment

An experimental treatment of AO7-spiked dye wastewater was carried out in order to assess the NGBC700's actual dye-wastewater treatment capability. Two dye-bearing wastewater samples were collected from a local dyer near Vasant Square Mall (28°31'31.3" N 77°09'20.7" E), New Delhi, India. The wastewater generated from the dyer is directly disposed of into the public sewer lines. The samples were collected in pre-cleaned 2 L polyethylene bottles. The dark red-colored sample was labeled "Sample R" while the dark blue-colored sample was labeled "Sample B". Physicochemical parameters including pH, EC, TDS, hardness, alkalinity, chloride, and sulfate contents were determined before and after the dye-wastewater treatment following the APHA guidelines. Both dye-wastewater samples were spiked with ~25 mg L<sup>-1</sup> of AO7. Additionally, 50 mL of each AO7-spiked dye wastewater sample was treated with NGBC700 (adsorbent dose = 3.0 g L<sup>-1</sup>; equilibrium time = 24 h) at 25 °C.

## 3. Results and Discussion

### 3.1. NGBC700 Characterization

The NGBC700's physicochemical properties are summarized in Table 2. The yield, moisture, and ash content of the NGBC700 are ~31%, ~6%, and ~21%, respectively. The carbon and oxygen contents of the NGBC700 are 62.8% and 30.5%, respectively. The BET surface area, pore radius, and total pore volume of the NGBC700 are 108 m<sup>2</sup> g<sup>-1</sup>, 19.13 Å, and 0.16 cm<sup>3</sup> g<sup>-1</sup>, respectively. The metal oxide contents (mg g<sup>-1</sup>) in the ash of NGBC700 are also reported in Table 2. The pH<sub>pzc</sub> of NGBC700 was estimated to be 8.9 (Figure S2). The biochar has a net positively charged surface at the dye solution's pH < 8.9.

**Table 2.** The proximate, ultimate, and metal contents of NGBC700.

Property/Element	Values
Yield (%)	~31
Ash (%)	~21
Moisture (%)	~6
Surface Area (S <sub>BET</sub> , m <sup>2</sup> g <sup>-1</sup> )	108
Total pore volume (cm <sup>3</sup> g <sup>-1</sup> )	0.16
Pore radius (Å)	19.13
Carbon (%)	62.8
Hydrogen (%)	1.94
Nitrogen (%)	4.20
Sulfur (%)	0.51
Oxygen (%)	30.5
MgO (mg g <sup>-1</sup> )	16.97
CaO (mg g <sup>-1</sup> )	46.25
K <sub>2</sub> O (mg g <sup>-1</sup> )	15.43
Al <sub>2</sub> O <sub>3</sub> (mg g <sup>-1</sup> )	1.18
Fe <sub>2</sub> O <sub>3</sub> (mg g <sup>-1</sup> )	1.17
MnO <sub>2</sub> (mg g <sup>-1</sup> )	0.22

SEM images revealed that the surface morphology of the biochar closely resembles a honeycomb structure marked by interwoven cylindrical pores alongside larger holes, as shown in Figure 2A,B [77]. The canal-like surface morphology of the NGBC700 contributes to its porosity. The lack of well-defined crystalline structures in TEM images confirms the amorphous nature of the biochar (Figure 2C,D). The graphitic carbon layer can be seen at the bottom left edge of Figure 2C.

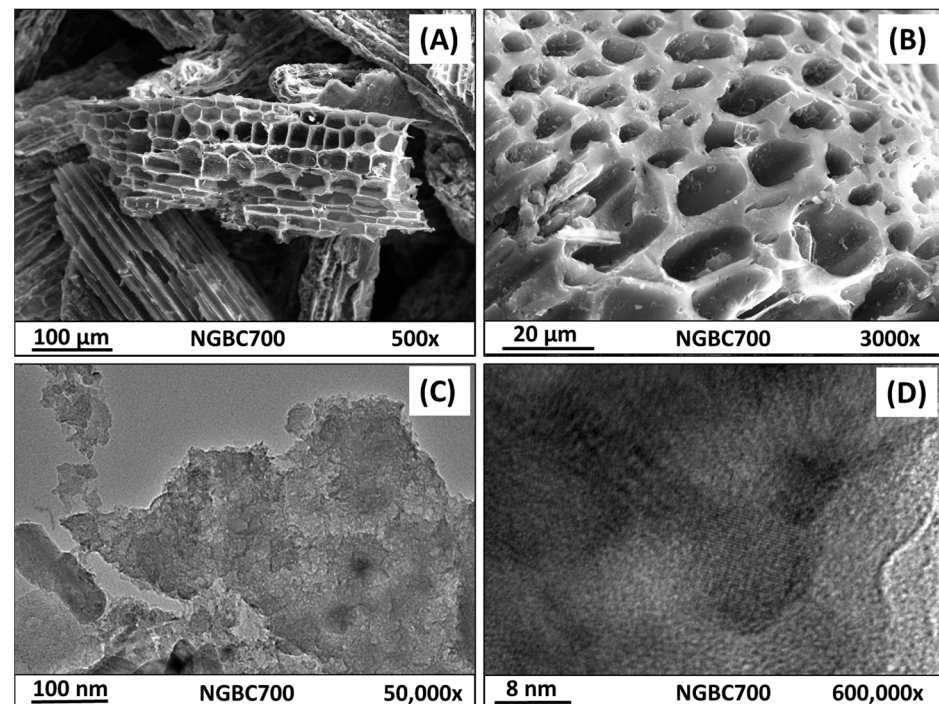


**Figure 2.** SEM images of NGBC700 at different magnifications: (A) 500x and (B) 3000x. TEM images of NGBC700 at different magnifications: (C) 50,000x and (D) 600,000x.

Figure 3 presents the SEM-EDX elemental maps and spectra of the NGBC700. The presence of carbon (43.8%), calcium (0.73%), magnesium (0.15%), potassium (0.30%), silicon (1%), and oxygen (54%) were observed after the SEM-EDX spectral analysis. The elemental results of the SEM-EDX analysis may vary from the bulk elemental composition results since they only revealed the surface (up to 2–3  $\mu\text{m}$ ) elemental content of the NGBC700 [68]. The color-coded elemental maps reveal their distribution on the NGBC700 surface.

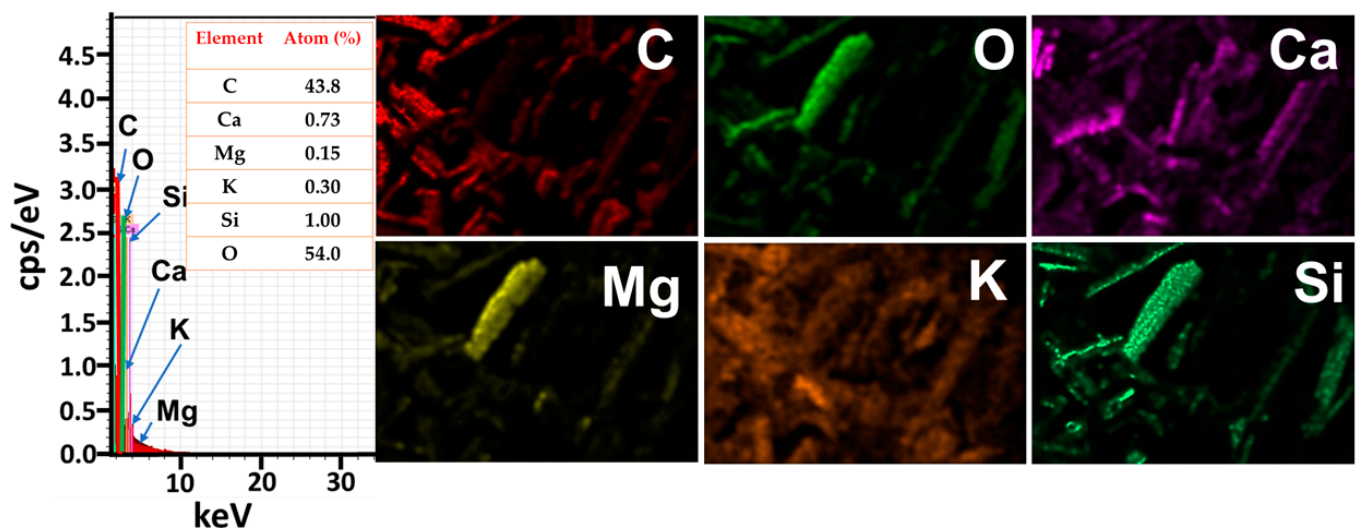


**Figure 3.** SEM-EDX spectra and mapping of NGBC700.

The FTIR spectra of NGBC700 and AO7-laden NGBC700 are shown in Figure 4. The minor peaks at  $871\text{ cm}^{-1}$  and  $1398\text{ cm}^{-1}$  are due to calcite in the biochar [78,79]. The C-O/C-O-C stretching frequency corresponds to  $1035\text{ cm}^{-1}$  [80]. In the AO7-laden NGBC700, a slight shift in the  $1035\text{ cm}^{-1}$  peak was reported, which may indicate the involvement of C-O/C-O-C groups in adsorption. The peak at  $1554\text{ cm}^{-1}$  is assigned to



aromatic C=C stretching [81–83]. The peak at  $2885\text{ cm}^{-1}$  is due to aliphatic C-H bond stretching vibration [84]. The prominent peaks observed within the infrared spectral range of  $3925\text{--}3500\text{ cm}^{-1}$  are ascribed to the stretching vibrations of –OH groups [85,86].

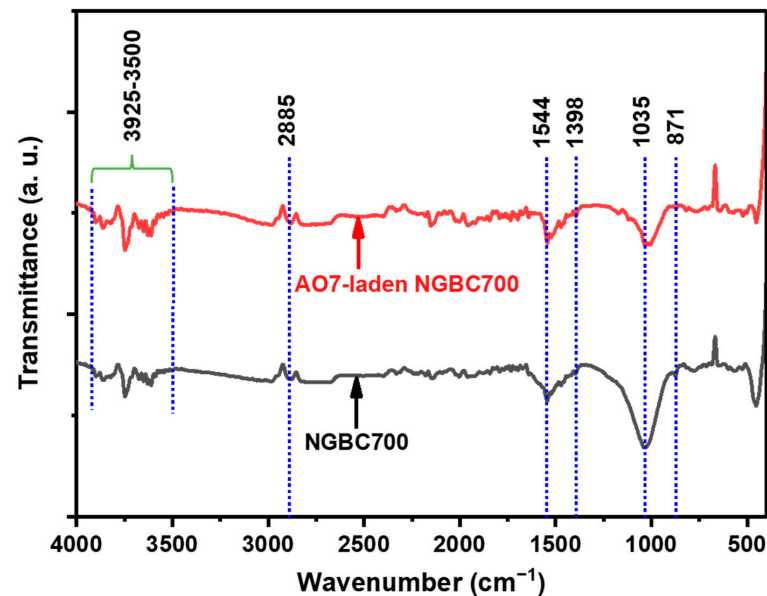


Figure 4. FTIR spectra of NGBC700 and AO7-laden NGBC700.

The XRD pattern of the NGBC700 is shown in Figure 5. A broad hump, peaking in the  $2\theta$  region of  $\sim 24^\circ$ , is due to the amorphous carbon present in the NGBC700 with a (002) reflection plane [85]. A sharp peak at  $2\theta = \sim 26.52^\circ$  ( $d = 3.323\text{ \AA}$ ) and a small peak at  $49.86^\circ$  ( $d = 1.781\text{ \AA}$ ) are attributed to the mineral quartz ( $\text{SiO}_2$ ) with corresponding (011) and (112) crystal planes, respectively [79,87,88]. The sharp peaks around  $2\theta = \sim 22.94^\circ$  ( $d = 3.852$ ),  $29.26^\circ$  ( $d = 3.037$ ),  $31.44^\circ$  ( $d = 2.825$ ),  $35.8^\circ$  ( $d = 2.493$ ),  $39.26^\circ$  ( $d = 2.252$ ),  $43.04^\circ$  ( $d = 2.082$ ),  $47.28^\circ$  ( $d = 1.936$ ),  $48.32^\circ$  ( $d = 1.897$ ),  $57.16^\circ$  ( $d = 1.608$ ), and  $60.62^\circ$  ( $d = 1.541$ ) reveal the presence of calcite in the NGBC700 with crystal planes at (012), (104), (006), (110), (113), (202), (024), (116), (122), and (214), respectively, as per JCPDS card no. 05–0586 and JCPDS card No. 47–1743 [50,89]. The dominance of calcite and quartz in the NGBC700 was also supported by SEM-EDX mapping and spectral data.

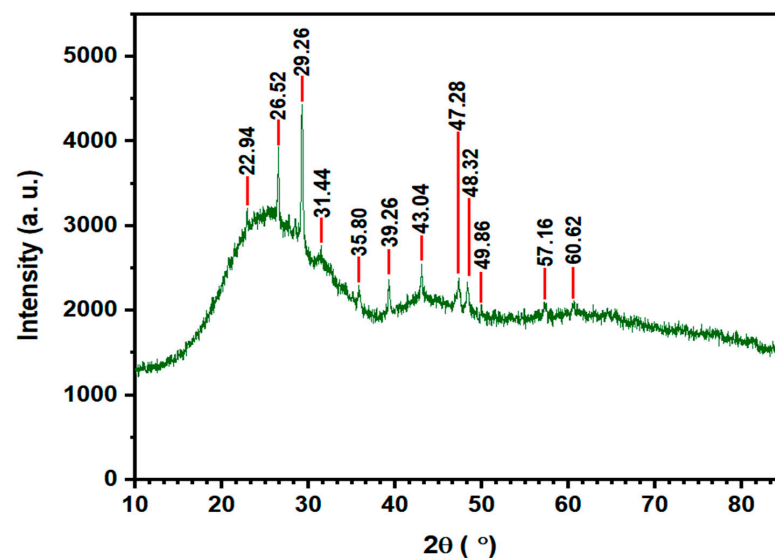
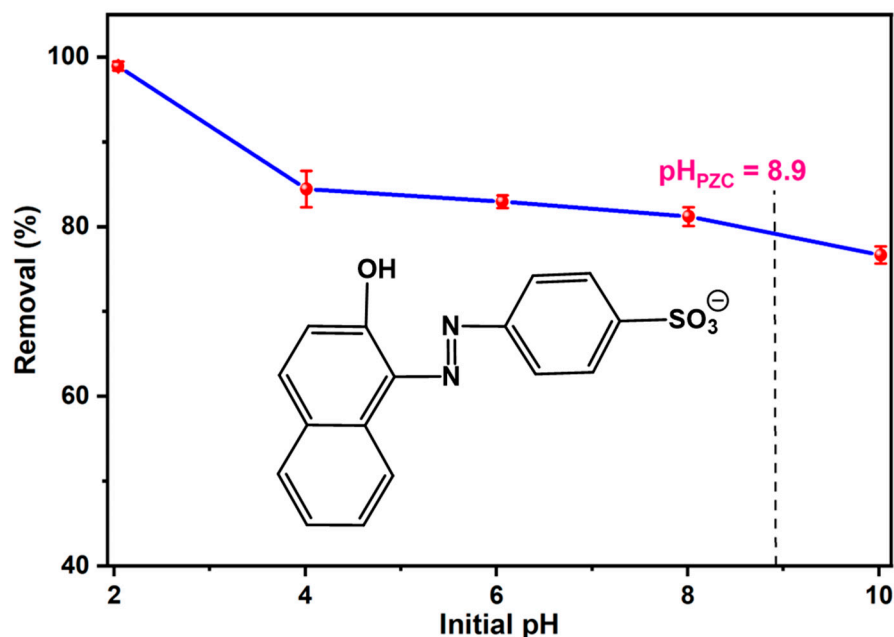


Figure 5. XRD spectrum of NGBC700.

### 3.2. Batch Study

#### 3.2.1. Effect of Solution pH

The effect of the initial solutions' pH on the sorption of AO7 onto the biochar is given in Figure 6. The  $pH_{pzc}$  of the prepared NGBC700 is  $\sim 8.9$ . On the other hand, the two  $pK_a$  values of the AO7 molecules are 1 for the  $-SO_3H$  group and 11 for the naphthalene group [90,91]. For aqueous solutions with pH values between 1 and 11, AO7 exists in a negatively charged monoprotinated form [90,91]. Due to electrostatic attraction between the anionic dye molecules and the NGBC700 surface, a lower pH ( $pH < \sim 8.9$ ) promotes AO7 adsorption by NGBC700 [90]. The removal efficiencies of AO7 on NGBC700 slightly decrease with an increase in solution pH. Similar results for AO7 sorption on other sorbents were also reported [42,48,92]. Removal efficiencies of 98.9%, 84.3%, 82.9%, 81.2%, and 76.6% were obtained at pH values of 2, 4, 6, 8, and 10, respectively. The highest removal efficiency (98.9%) was recorded at an initial pH of 2. The availability of significant  $H^+ / H_3O^+$  ions at the adsorbent surface at a very low pH ( $pH = 2$ ) facilitates the electrostatic attraction between AO7 molecules ( $SO_3^-$  group) and the  $H^+ / H_3O^+$ -charged adsorbent's surface [42,90,92]. However, no significant difference in the removal of AO7 on NGBC700 at initial pH values of 4 (84.3%), 6 (82.9%), and 8 (81.2%) was observed. At a pH of 10, the AO7 removal efficiency was the lowest due to electrostatic repulsions between anionic AO7 molecules and the net negatively charged NGBC700 surface ( $pH_{pzc} = \sim 8.9$ ) [42,92]. Given that wastewater typically falls within a pH range of 6–10, a pH of 6.5 was selected for further kinetic and equilibrium studies [93].



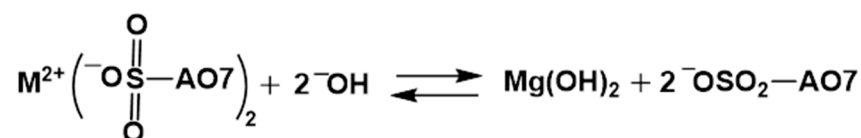
**Figure 6.** Effect of pH on the adsorption of AO7 on NGBC700.

#### 3.2.2. AO7 Sorption Interactions

Spectroscopic analyses were employed to propose sorption interactions between the AO7 and NGBC700 surfaces. During the NGBC700 preparation,  $Ca^{2+}$  and  $Mg^{2+}$  salts (Table 2) were converted into  $CaO$ ,  $Ca(OH)_2$ ,  $CaCO_3$ ,  $MgO$ , and  $Mg(OH)_2$ . Thus, inside and at the surface, these basic inorganics exist and contribute to pushing the surface to become more basic, while phenolic, carboxylic groups are acidic. Acid orange 7 in water is mostly ionized to  $AO7 - SO_3^-$ , and this can interact with  $Mg(OH)_2$ ,  $MgO$ ,  $CaO$ ,  $Ca(OH)_2$ ,

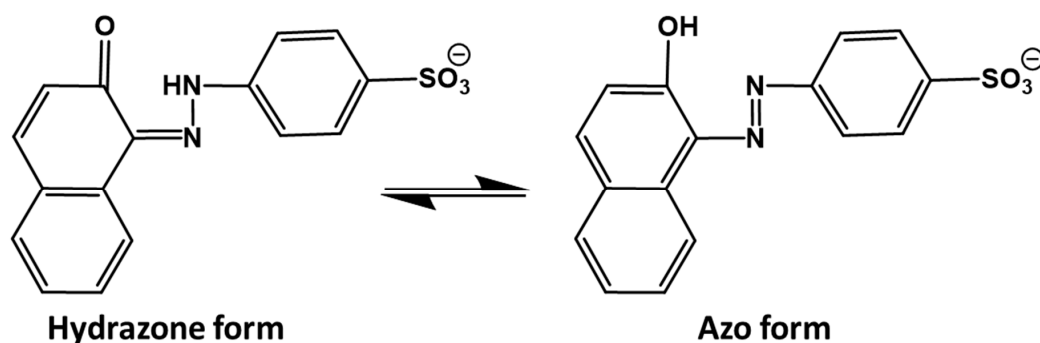
and carbonate. This can give  $Ca^{2+}$  and  $^-OSO_2-AO7$  sites.  $Ca^{2+}$  and  $Mg^{2+}$  and carbonate. This can give  $Ca^{2+}$  and  $^-OSO_2-AO7$  sites.  $Ca^{2+}$  and  $Mg^{2+}$  can form and be part of what is adsorbed.  $CaSO_4$  and  $MgSO_4$  are soluble, but when a larger

organic group is present, it lowers the solubility of these salts. Such salts can form on the surfaces of the  $\text{CaCO}_3$  and  $\text{MgO}$  in the NGBC700. This is true over most of the pH range, but as the pH increases, the following reaction may take place.

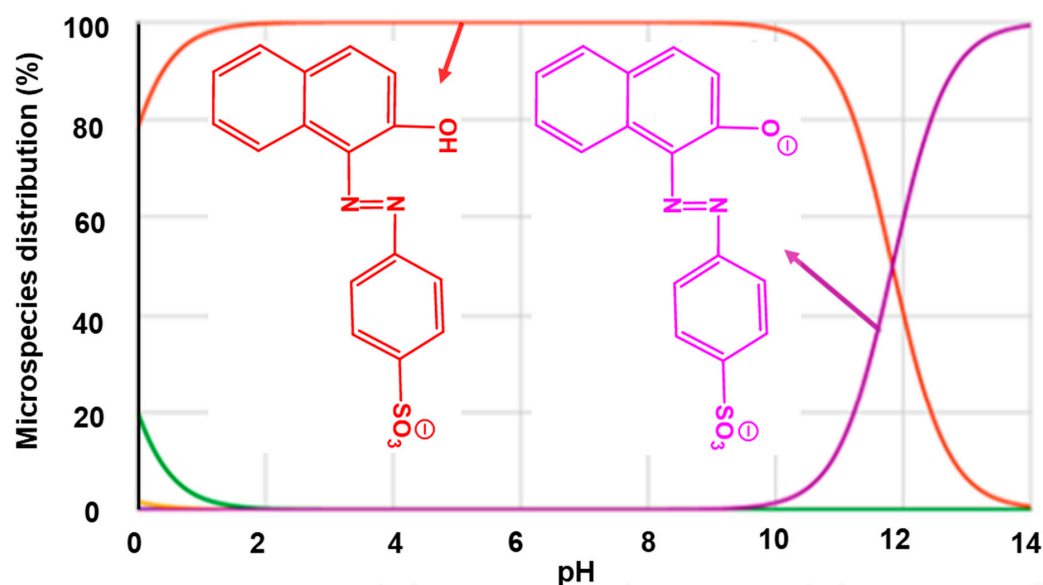


This agrees with some drop in the removal percentage versus pH, as can be seen in Figure 6.

Additionally, AO7 primarily exists in azo and hydrazone tautomeric forms (Scheme 1). In an aqueous solution, the hydrazone form dominates [94]. AO7 has two pKa values ( $\text{pK}_{\text{a}1} = 1$  for the  $-\text{SO}_3\text{H}$  group and  $\text{pK}_{\text{a}2} = 11$  for the naphthalene group) [90,91]. From pH values of 1 to ~11, AO7 exists in a negatively charged monoprotinated form [90,91]. AO7 will be negatively charged at  $\text{pH} > 11$ , (Scheme 2). The NGBC700 has a  $\text{pH}_{\text{pzc}}$  of ~8.9. Thus, the NGBC700 surfaces are net positively charged at  $\text{pH} < 8.9$ , while they become net negative  $> \text{pH} 8.9$ .



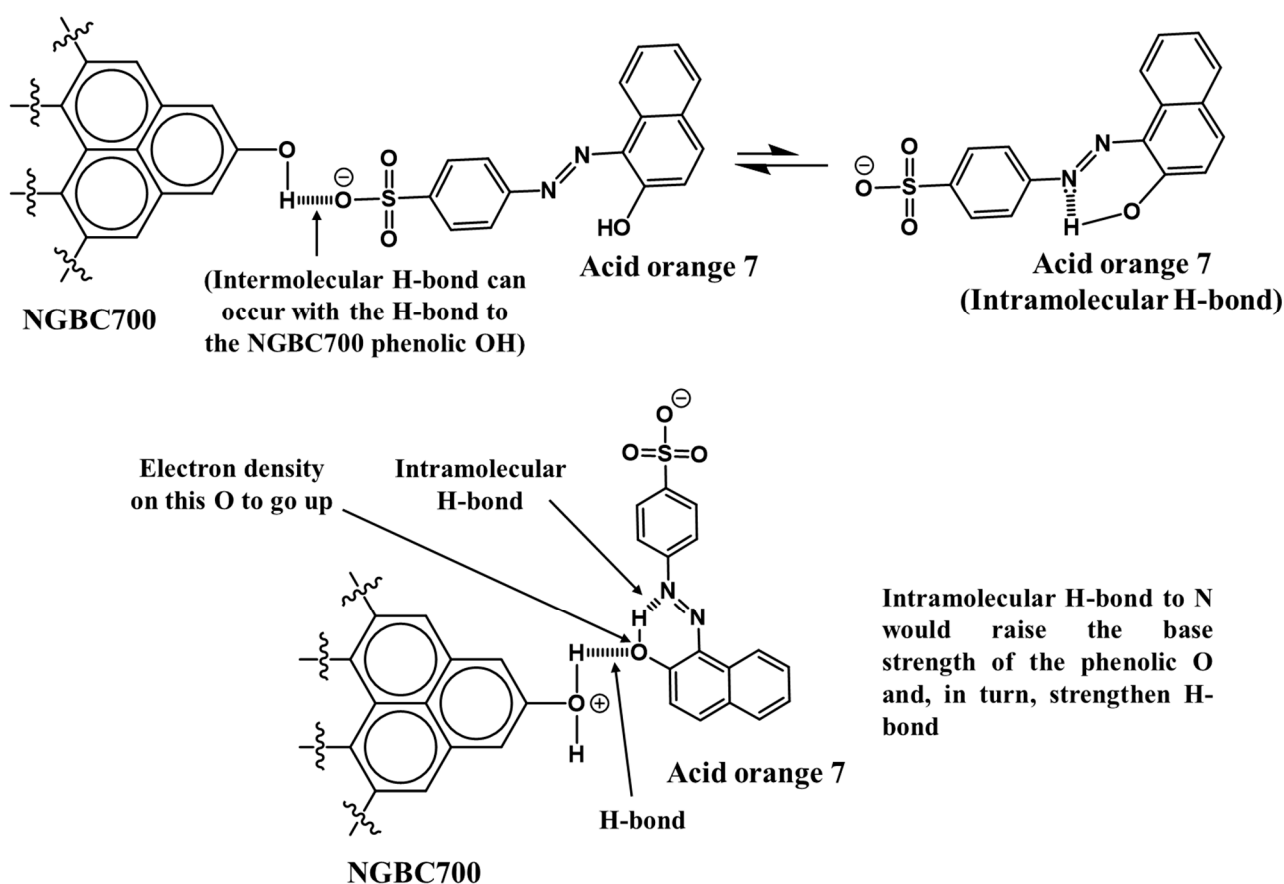
**Scheme 1.** AO7 tautomeric forms in an aqueous solution, adopted with permission from Ref. [95]. Copyright 2003, Elsevier.



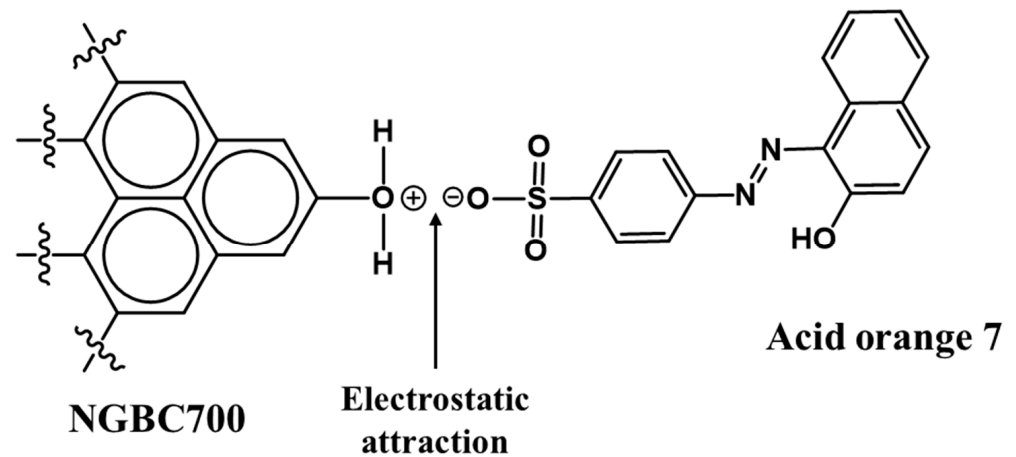
**Scheme 2.** Acid orange 7 speciation in aqueous media, adopted with permission from Ref. [96]. Copyright 2020, Elsevier.

The anionic AO7 species is electrostatically attracted toward the protonated NGBC700 surfaces, leading to high adsorption in the acidic solution (Figure 6). The positively charged NGBC700 surface promoted anionic AO7 adsorption at  $\text{pH} < \text{pH}_{\text{pzc}}$ . A proton was also lost by the AO7 molecule when the pH was raised above 10, making it more difficult to connect to the negatively charged NGBC700. Furthermore, the AO7 molecule undergoes increased tautomerization with a rise in the solution pH [97]. Scheme 1 illustrates how intramolecular proton transfer from the hydroxyl group to one of the nitrogen atoms in the azo group may occur. In aqueous solutions at relatively higher pH levels, the hydrazine tautomer emerges as the predominant AO7 form. In this tautomer, the ketal group may reduce the sorption capacity due to its weaker interaction with the NGBC700 versus the azo tautomer as it lacks hydrogen bonding at the oxygen atom of the substrate [97].

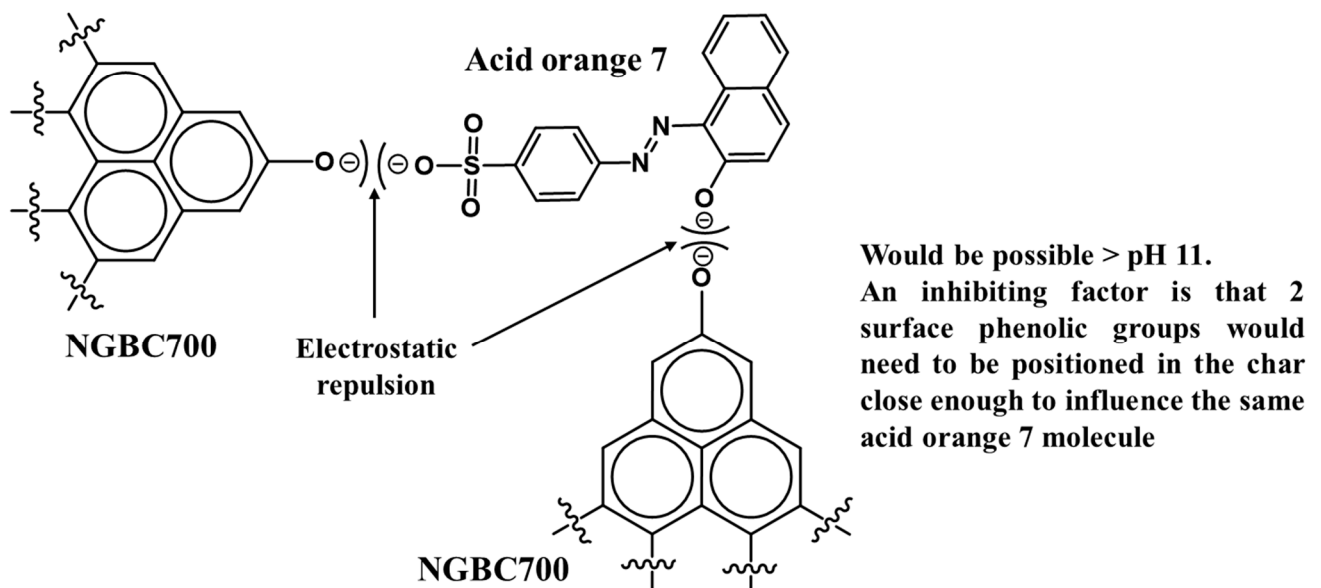
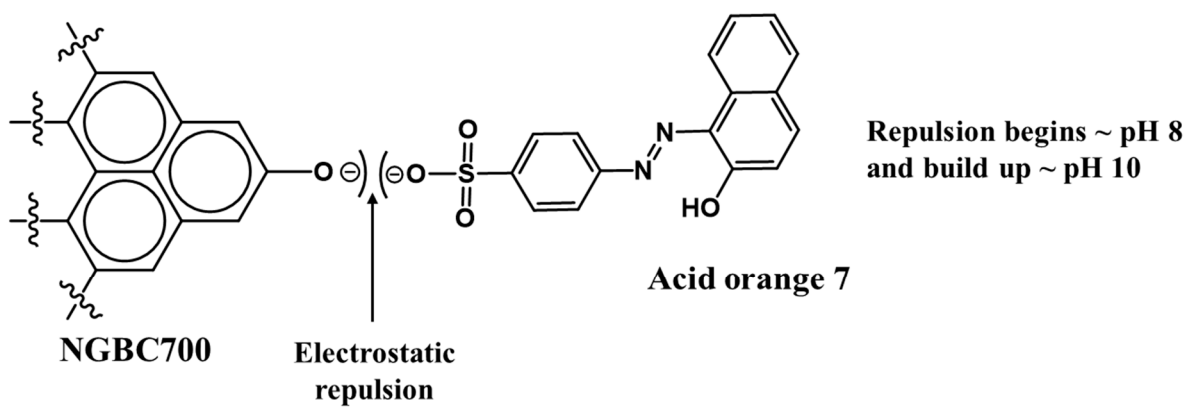
An anionic AO7 can form hydrogen bonds with carbonyl, hydroxyl, ether, phenolic, and quinoid/keto groups that are present on the NGBC700. H-bonding between anionic AO7 and protonated and neutral NGBC700 surfaces can exist at  $\text{pH} < 8.9$  (Scheme 3). The electrostatic attraction between protonated NGBC700 surfaces and negatively charged AO7 is possible at a very low pH (Scheme 4). The electrostatic repulsions between negatively charged NGBC700 surfaces with mono-anionic and di-anionic AO7 (Scheme 5) occur when  $\text{pH} = 8.9\text{--}11$  and  $>11$ , respectively. The electron-deficient aromatic portions of the AO7 molecule could result in  $\pi$  donor–acceptor interactions with  $\pi$  electron-rich phenoxide groups of NGBC700 (Scheme 6). ?? 3–6 list only a handful of the many enticing interactions that exist between AO7 and NGBC700. Over a wide range of pH values, much more could be offered.



**Scheme 3.** Possible hydrogen bond formation between NGBC700 (neutral and protonated) surfaces and anionic acid orange 7.

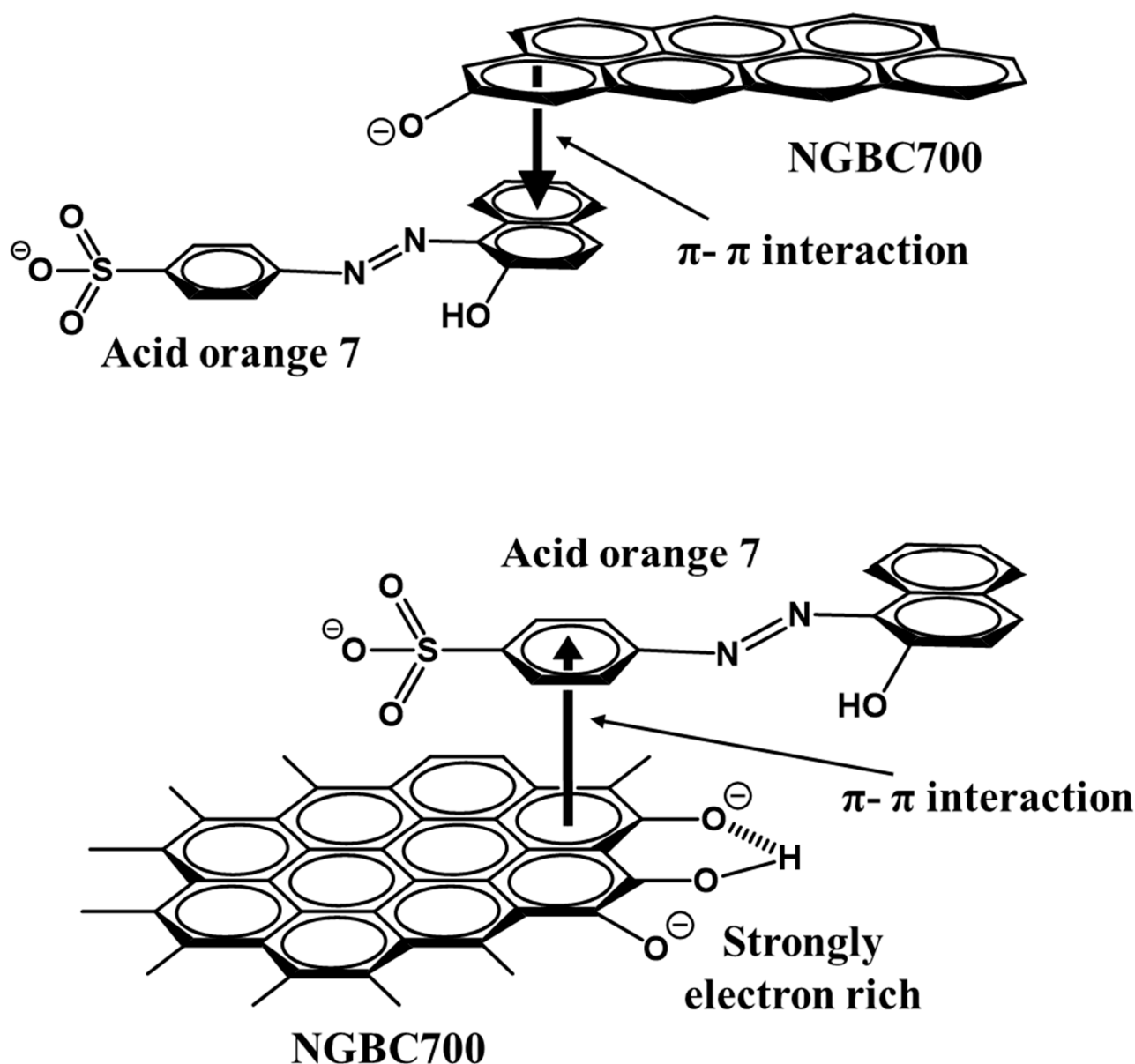


**Scheme 4.** Electrostatic attraction between positively charged NGBC700 surface and anionic acid orange 7 (under very acidic pH).



**Scheme 5.** Electrostatic repulsions between anionic acid orange 7 and negatively charged NGBC700 surface.





**Scheme 6.**  $\pi$ - $\pi$  electron donor-acceptor attractions between NGBC700's aromatic rings and anionic acid orange 7.

### 3.2.3. Effect of NGBC700 Doses on AO7 Sorption Kinetics

The dye removal performance of different doses of the NGBC700 over different time intervals is shown in Figure 7A. At an initial  $10 \text{ mg L}^{-1}$  AO7 conc., the percent dye removal was enhanced from 60.2 to 89.9% when the biochar dose was raised from 1 to  $2 \text{ g L}^{-1}$  at  $25^\circ \text{C}$  after 24 h, respectively. The AO7 adsorption rate increased rapidly up to the first 8 h and then rose very slowly for the next 48 h. The reason for this trend may be attributed to the fact that the sites available for adsorption on the biochar's surface decrease owing to interactions between the AO7 and the NGBC700's surface [33,92,98]. However, a further increase in biochar dose from 3 to  $4 \text{ g L}^{-1}$ , does not significantly increase the percent dye removal. The equilibrium time for the sorption of AO7 onto the biochar was  $\sim 10 \text{ h}$ . Thus, all sorption experiments were carried out at an optimum biochar dose of  $2 \text{ g L}^{-1}$ . An equilibrium sorption time of 24 h was taken to ensure the complete exhaustion of biochar.

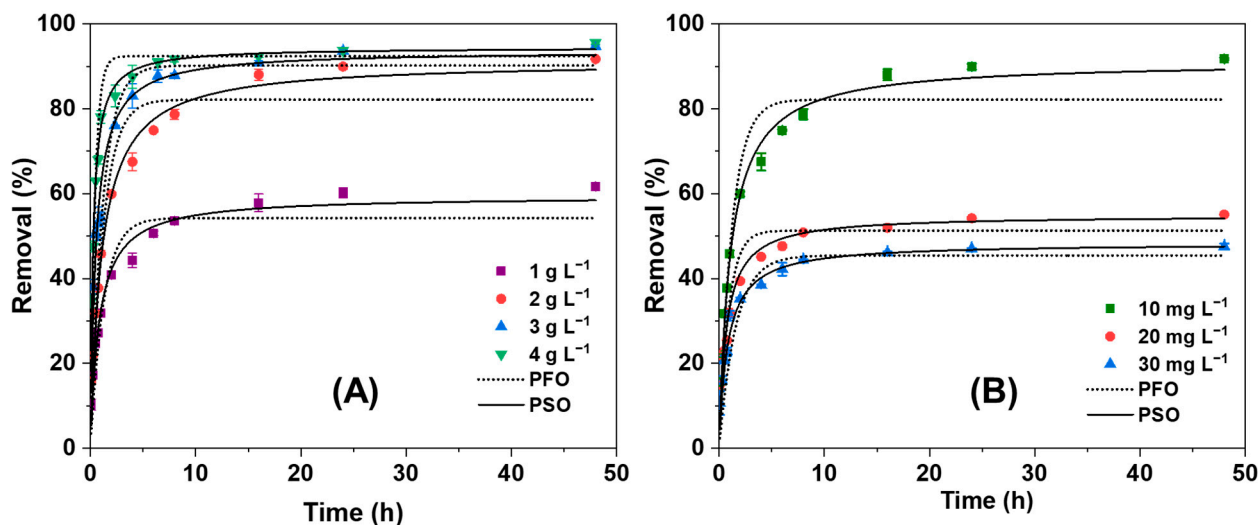


**Figure 7.** Sorption kinetic data fittings for (A) different NGBC700 doses on AO7 removal efficiencies and (B) different initial AO7 concentrations on dye removal efficiencies. Experimental data are represented by points, while dotted and solid lines represent PFO and PSO kinetic equation fittings to experimental data, respectively [particle size = 52–100 BSS; pH = 6.5; biochar dose = 2 g L<sup>-1</sup>; initial AO7 concentration = 10 mg L<sup>-1</sup>; agitation speed = 100 rpm; temp. = 25 °C].

The sorption kinetic data were fitted to the PFO and the PSO (Figure 7A) kinetic equations. All rate constants obtained from the fittings of data to the PFO and the PSO equations are summarized in Table 3. The sorption kinetic data fitted the PSO equation more accurately ( $R^2 = 0.969$ – $0.997$ ) vs. the PFO equation ( $R^2 = 0.789$ – $0.988$ ). The higher correlation coefficients for the PSO explain that the sorption of AO7 onto the NGBC700 was a function of the dye concentration and biochar quantity, and the reaction was influenced by the abundance of the biochar's surface-active sites [33,92]. The better fitting of the sorption data onto the PSO indicated that chemical sorption is the rate-limiting step in the sorption of AO7 onto the biochar [99]. The AO7 percentage removal values from the experimental data are much closer to those obtained using the PSO equation vs. the PFO equation. The pseudo-second-order rate constant at the optimized dose is 0.21 g mg<sup>-1</sup> h<sup>-1</sup>.

**Table 3.** AO7 sorption kinetic data.

Biochar Dose (g L <sup>-1</sup> )	Calculated q <sub>e</sub> (%)	PFO			PSO		
		q <sub>e</sub> (%)	k <sub>1</sub> (h <sup>-1</sup> )	R <sup>2</sup>	q <sub>e</sub> (%)	k <sub>2</sub> (g mg <sup>-1</sup> h <sup>-1</sup> )	R <sup>2</sup>
1	61.7	54.2	0.80	0.918	59.4	0.20	0.983
2	91.8	82.1	0.82	0.964	91.2	0.21	0.994
3	94.8	90.2	0.86	0.789	93.7	0.63	0.969
4	95.6	92.4	2.29	0.988	94.5	1.7	0.997
Dye conc. (mg L <sup>-1</sup> )							
10	91.7	82.2	0.82	0.964	91.2	0.21	0.994
20	55.1	51.3	1.11	0.915	54.9	0.27	0.968
30	47.6	45.4	0.63	0.806	48.3	0.17	0.964

### 3.2.4. Effect of Initial Dye Concentration on Sorption Kinetics

The effects of the initial dye concentration on sorption kinetics are shown in Figure 7B. The percent dye removal decreased (91.8% → 55.1% → 47.6%) with increased initial dye concentrations (10 mg L<sup>-1</sup> → 20 mg L<sup>-1</sup> → 30 mg L<sup>-1</sup>) at 48 h. The percent AO7 removal rate increased rapidly during the first 8 h. After 8 h, the removal rate (%) rose very slowly owing to the lesser availability of adsorption sites due to greater site occupancy by dye

molecules during the initial hours [33,92]. In this case, the equilibrium time for the sorption of AO7 onto NGBC700 is ~12 h.

The sorption kinetic data were also fitted to the PFO and the PSO (Figure 7B) kinetic equations. All parameters obtained after the kinetic equation fittings are summarized in Table 3. Again, the PSO ( $R^2 = 0.964$ – $0.994$ ) equation was preferred over the PFO ( $R^2 = 0.806$ – $0.964$ ) equation. The better fitting of kinetic sorption to the PSO revealed that chemical sorption is the rate-limiting step [99,100].

### 3.2.5. Sorption Isotherm Study

Equilibrium studies for the sorption of AO7 onto the NGBC700 were performed at 10, 25, and 40 °C (Figure 8). Experimental isotherm data were fitted to the Langmuir and Freundlich isotherm models. The different parameters of the Langmuir and Freundlich isotherm models for AO7 sorption onto the NGBC700 are tabulated in Table 4. The monolayer Langmuir capacities for AO7 sorption on the NGBC700 were 14.3, 12.7, and 8.4 mg g<sup>−1</sup> at 10, 25, and 40 °C, respectively. This reduction in sorption capacity with an increase in temperature suggests an exothermic nature of AO7 sorption on NGBC700.

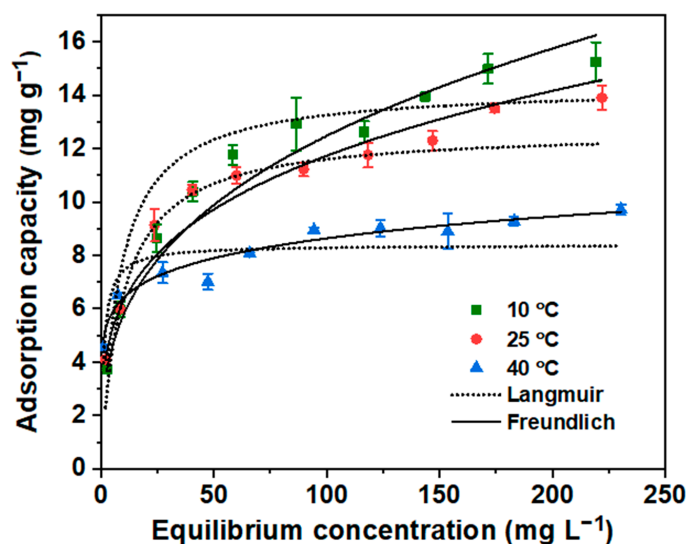


**Figure 8.** AO7 sorption equilibrium data fitting to the Freundlich and Langmuir isotherm models. Experimental data are represented by points, while dotted and solid lines represent Langmuir and Freundlich isotherms fitting to experimental data, respectively [particle size = 52–100 BSS; pH = 6.5; NGBC700 dose = 2 g L<sup>−1</sup>; agitation speed = 100 rpm; temperature = 10, 25, and 40 °C].

**Table 4.** Isotherm parameters for AO7 sorption onto NGBC700 at 10, 25, and 40 °C.

Isotherm Model	Parameters	Temperature		
		10 °C	25 °C	40 °C
Langmuir	Q° (mg g <sup>−1</sup> )	14.3	12.7	8.4
	b (L mg <sup>−1</sup> )	0.12	0.11	0.77
	R <sup>2</sup>	0.987	0.788	0.831
	Reduced $\chi^2$	10	139	32
Freundlich	K <sub>F</sub> (mg g <sup>−1</sup> )	2.65	3.36	4.75
	n	2.98	3.68	7.69
	R <sup>2</sup>	0.994	0.987	0.965
	Reduced $\chi^2$	4.4	8	6.7

The AO7 sorption equilibrium data fit the Freundlich equation ( $R^2 = 0.965$ – $0.994$ ) better than the Langmuir equation ( $R^2 = 0.788$ – $0.987$ ). This observation was further supported by smaller reduced  $\chi^2$  value obtained from the Freundlich isotherm (reduced  $\chi^2 = 4.4$ – $8$ )

compared to the Langmuir isotherm (reduced  $\chi^2 = 10\text{--}139$ ) at 10, 25, and 40 °C. The better fitting of the AO7 sorption data to the Freundlich isotherm suggests multilayer AO7 sorption on the heterogeneous surface of the NGBC700 [33,67]. Furthermore, the distribution of active sites on the NGBC700 is non-uniform, and interactions between these active sites and AO7 have differential affinities based on adsorption heat [101]. Such interactions are typically obtained for the adsorption of organic compounds onto activated carbon or a similar adsorbent [101].

### 3.2.6. NGBC700 Regeneration/ AO7 Desorption

Adsorption treatment is more economical when the sorbent can be reused [66,67]. To determine the biochar's technical, commercial, and recyclable viability, desorption experiments were carried out (Figure 9). AO7 desorption was initially carried out with 0.1 N NaOH, 0.1 N HCl, 0.1 N NaCl, and 10% EtOH. (Figure 9A). Maximum AO7 removal (~35%) was achieved using NaOH (0.1 N) vs. 0.1 N HCl (23%), 0.1 N NaCl (11%), and 10% ethanol (18%). Further, regeneration studies were performed for three adsorption–desorption cycles using 0.01, 0.05, 0.1, 0.5, and 1 N NaOH (Figure 9B). No significant differences in AO7 removal were seen when using 0.01, 0.05, and 0.1 N NaOH. The AO7 removal efficiencies of NGBC700 after the 0th, 1st, 2nd, and 3rd cycles were 56.5, ~35, 33.1, and 29%, respectively, when treated with 0.1 N NaOH. The 0th cycle indicates that no desorption was carried out. The 1st, 2nd, and 3rd cycles refer to AO7 adsorption on NGBC700 after desorption of AO7 adsorbed during the previous 0th, 1st, and 2nd cycles, respectively. Similar AO7 removal trends were obtained with 0.01 and 0.05 N NaOH. With 0.5 N NaOH (0th cycle = 56.5%, 1st cycle = 47%, 2nd cycle = 44.3%, and 3rd cycle = 42.2%) and 1 N NaOH (0th cycle = 56.3%, 1st cycle = 50.1%, 2nd cycle = 48.7%, and 3rd cycle = 47.5%), AO7 removal was higher in each cycle versus when using 0.01, 0.05, and 0.1 N NaOH. Thus, 0.5 N NaOH was selected for further studies as the best eluent to desorb AO7 from NGBC700.

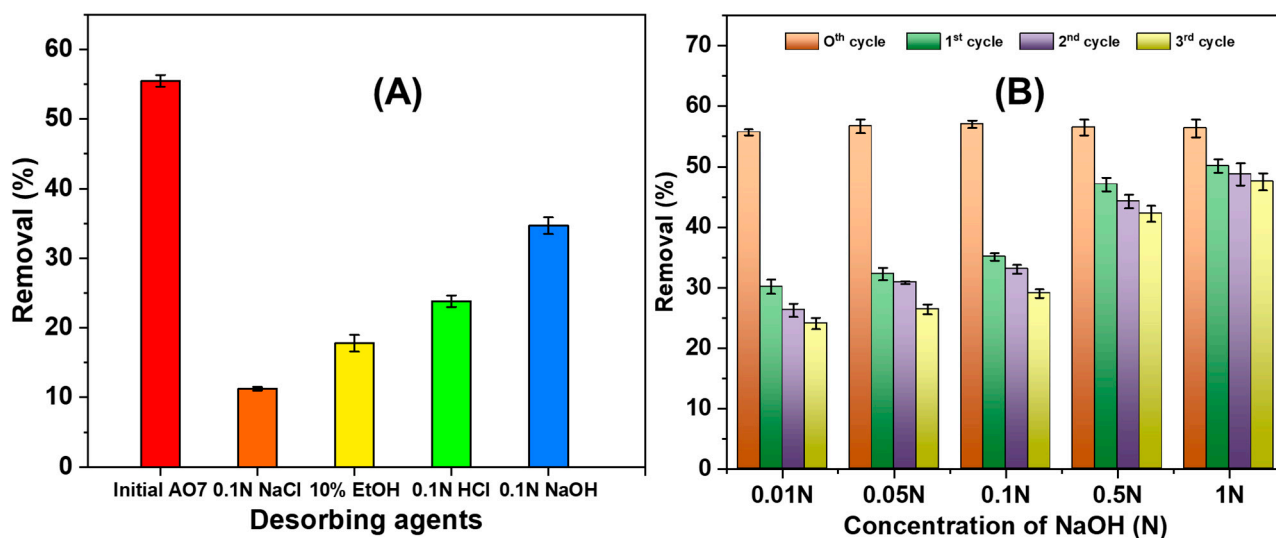


**Figure 9.** NGBC700 regeneration: (A) screening study and (B) 3 adsorption–desorption cycles using 0.01, 0.05, 0.1 N, 0.5 N, and 1 N NaOH.

### 3.2.7. Acid Orange 7 Sorption Capacities on NGBC700 vis-à-vis Other Adsorbents

A comparison of the AO7 sorption capacities of the NGBC700 and other adsorbents is summarized in Table 5. Different adsorbents prepared from tea residue, sorghum straw, rice husk, activated carbon, lemon peel, pulp, and waste sludge were utilized to treat AO7. The AO7 adsorption capacity per unit surface area of the NGBC700 was lower or comparable to many other adsorbents. Adsorbents with a higher AO7 sorption capacity were mostly modified (physical or chemical), whereas we used low-cost, pristine NGBC700.

**Table 5.** Acid orange 7 sorption capacities on NGBC700 vs. other adsorbents.

Adsorbents	Surface Area (m <sup>2</sup> g <sup>−1</sup> )	pH	Temp. (°C)	Maximum Adsorption Capacity (mg g <sup>−1</sup> )	Adsorption Capacity per Unit Surface Area (mg m <sup>−2</sup> )	Reference
Napier grass biochar (NGBC700)	108	6.5	10	14.3	0.13	This study
			25	12.7	0.12	
			40	8.4	0.08	
NaOH-modified tea residue biochar	178	2	25	96.71	0.54	[102]
			5	25.15	0.11	
Fe-sorghum straw biochar	216.6	6	15	28.91	0.13	[96]
			25	59.34	0.27	
CaO/CeO <sub>2</sub> composite	32.3	2	28	27.78	0.86	[103]
Sludge-rice husk biochar	29.18	6–7	25	42.12	1.45	[104]
Zeolitic imidazolate framework-8	978	6	25	80.47	0.08	[105]
Milk-vetch shrub activated carbon	565	7	25	99	0.18	[106]
Activated carbon fiber	842	-	30	230	0.27	[107]
Lemon peel biochar	194.7	2	-	225	1.15	[47]
Modified multi walled carbon nanotubes	1800	7	25	59.52	0.03	[108]
<i>Cucumis sativa</i> peel biochar	NA	2	25	11.21	NA	[49]
Granular activated carbon	704.23	3	30	665.9	0.94	[97]
Co-pyrolyzed shaddock peel and red mud	93.51	2.2	25	32	0.34	[48]
Activated carbon	878	6	25	109.05	0.12	[109]
Triethylenetetramine (TETA)-treated sulfonated mandarin biochar	5.98	2	25	312.5	52.25	[15]
Core-shell-structured NH <sub>2</sub> functionalized UiO-66 magnetic composites	722.6	NA	25	48.12	0.06	[110]
Fe <sub>3</sub> O <sub>4</sub> -modified sewage sludge biochar prepared at 450 °C	127.98	2	25	110.27	0.86	[111]
Fe <sub>3</sub> O <sub>4</sub> -modified sewage sludge biochar prepared at 700 °C	99.83			64.40	0.64	
De-inked Pulp Waste Sludge Activated Carbon (DIPSAC)	1523.7	2	30	12.88	0.008	[112]
			40	12.33	0.008	
			50	12.23	0.008	



### 3.3. Column Study

The breakthrough curve plays a pivotal role in assessing column performance [33,67]. Table 6 summarizes the column parameters of AO7 sorption on the NGBC700 derived from the breakthrough curve (Figure 10A). The column's capacity for AO7 sorption ( $4.4 \text{ mg g}^{-1}$ ) was notably lower compared to values obtained from batch sorption studies ( $12.7 \text{ mg g}^{-1}$ ) performed at approximately the same temperature ( $\sim 27^\circ \text{C}$ ). This discrepancy can be largely attributed to the brief contact time (EBCT = 7.85 min) between the adsorbent and adsorbate in the column [67]. The breakthrough volume was 460 mL, with exhaustion occurring at 1665 mL. Furthermore, breakthrough was observed at 89 min, while exhaustion took place at 367 min. The NGBC700 usage rate was  $8.7 \text{ g L}^{-1}$ .

**Table 6.** Column parameters calculated for AO7 sorption on NGBC700.

Column Parameters	Values
Weight of NGBC700 (g)	4
Bed volume ( $\text{cm}^3$ )	34.54
EBCT (Empty bed contact time) (min)	7.85
NGBC700 usage rate ( $\text{g L}^{-1}$ )	8.7
Column capacity ( $\text{mg g}^{-1}$ )	4.4
Initial concentration ( $\text{mg L}^{-1}$ )	20
Concentration at exhaustion point ( $C_x$ ) ( $\text{mg L}^{-1}$ )	18
Concentration at breakthrough point ( $C_b$ ) ( $\text{mg L}^{-1}$ )	2
Exhaustion volume ( $V_x$ ) (mL)	1665
Breakthrough volume ( $V_b$ ) (mL)	460
Total time to reach exhaustion point ( $t_x$ ) (min)	367
Total time to reach breakthrough ( $t_b$ ) (min)	89
Percent saturation (%)	73.5
Fractional capacity (f)	0.65
Primary adsorption zone (cm)	8.33

The continuous AO7 sorption data were fitted to Thomas and Yoon–Nelson models (Figure 10B,C). Table 7 provides the Yoon–Nelson and Thomas model parameters. The experimental data moderately fit the Thomas ( $R^2 = 0.76$ ) and Yoon–Nelson models ( $R^2 = 0.76$ ) for continuous AO7 sorption on NGBC700. The AO7 adsorption capacity obtained using Thomas model ( $5.2 \text{ mg g}^{-1}$ ) closely matched the experimental column capacity ( $4.4 \text{ mg g}^{-1}$ ), confirming the Thomas model's applicability to the column data. Likewise, the  $T_{0.5}$  calculated using the Yoon–Nelson model (239 min) was in close agreement with the experimental value of 215 min (Table 7). These findings suggest the utility of these models in designing columns for scale-up processes.

**Table 7.** Column model parameters for AO7 sorption on NGBC700.

Thomas Model			Yoon–Nelson Model			Experimental Data	
$K_{TH}$ (mL/min.mg)	$q_{max}$ ( $\text{mg g}^{-1}$ )	$R^2$	$K_{YN}$ ( $\text{min}^{-1}$ )	$T_{0.5}$ (min)	$R^2$	$q_{e\text{-exp}}$ ( $\text{mg g}^{-1}$ )	$T_{0.5\text{-exp}}$ (min)
1.09	5.2	0.76	0.0216	239	0.76	4.4	215

### 3.4. Actual Dye Wastewater Treatment

Dye-based industries, especially small and medium-sized ones, dispose of their untreated wastewater in streams due to budgetary constraints [113]. NGBC700 was used to completely remove AO7 from locally available dye wastewater. Dye wastewater physicochemical parameters before and after contamination are given in Table S2. The AO7 removal efficiencies using the NGBC700 from sample R and sample B are given in Figure 11. AO7 removal efficiencies of approximately 100% were achieved by the NGBC700 for the AO7-spiked sample R and sample B. Thus, the developed NGBC700 has potential to be used in the decolorization of AO7-laden dye wastewater.

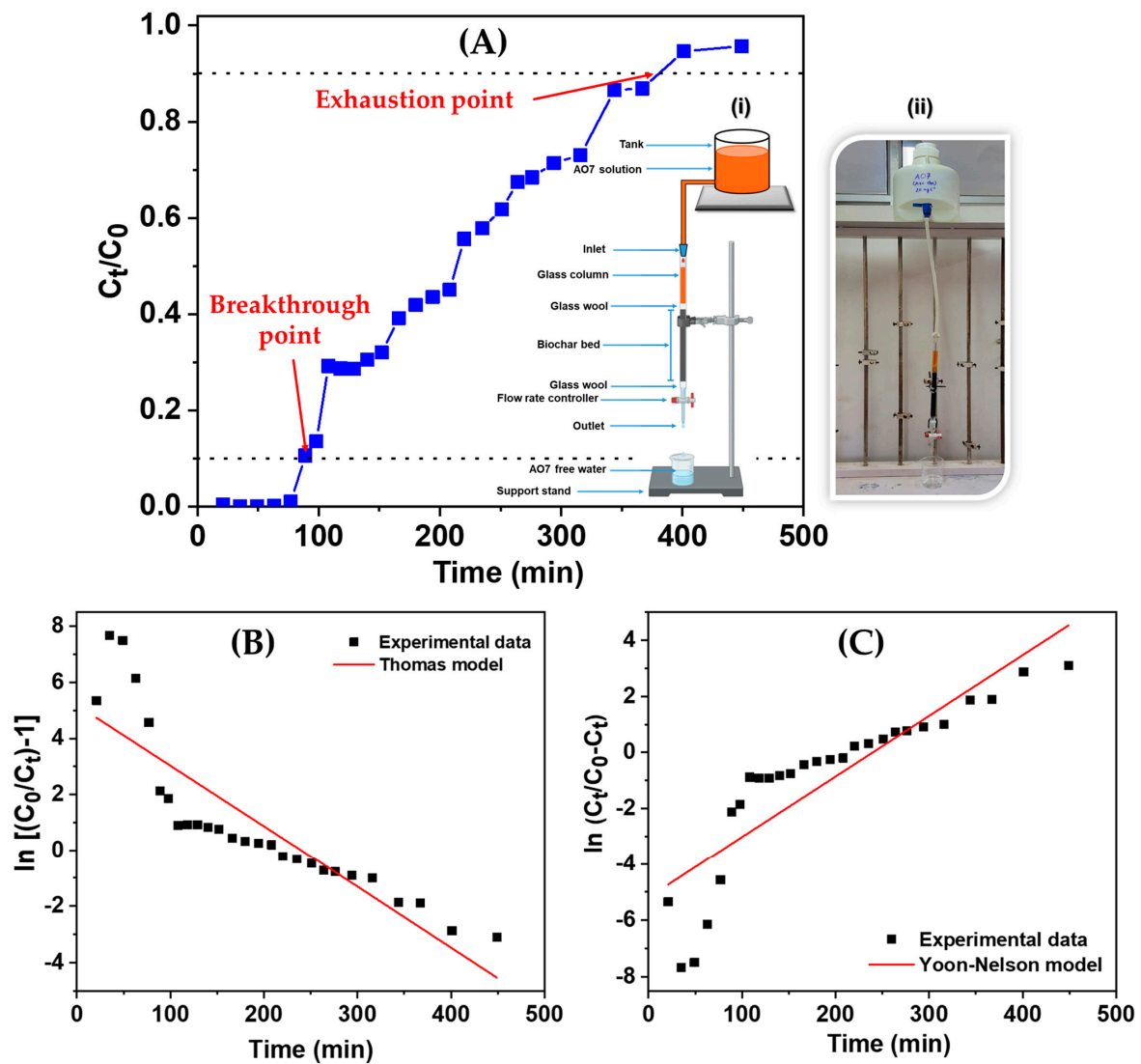


Figure 10. (A) Breakthrough curve of AO7 sorption on NGBC700: (i) schematic column setup and (ii) actual column setup. Fixed-bed data fitting of (B) Thomas model and (C) Yoon–Nelson model.

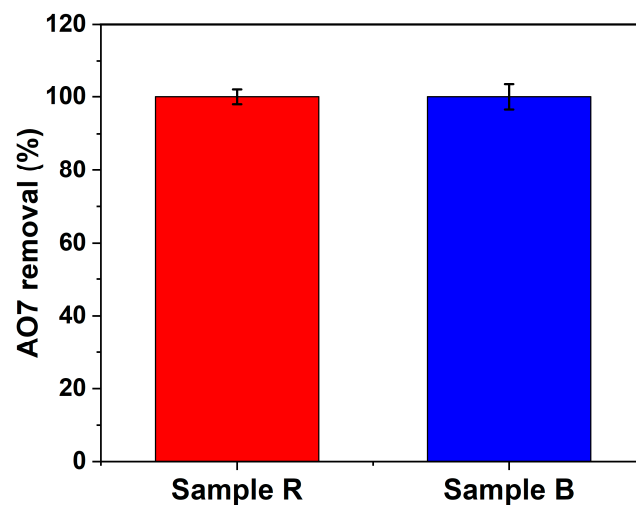


Figure 11. NGBC700-assisted AO7 removal from spiked dye wastewaters (sample R and sample B) [volume of AO7-spiked samples R or B = 50 mL; NGBC700 dose = 0.15 g; agitated at 100 rpm; equilibrium time = 24 h; temp. = 25 °C].

#### 4. NGBC700 Preparation Cost

The NGBC700 preparation cost was calculated as per the equation given in Section 2.7. Table S3 summarizes the NGBC700 preparation cost in US\$ and IN₹. The detailed costs of biochar preparation, as per the equation, are given step-wise below:

$$\text{COST}_{\text{BC}} = \text{US\$ } 1.62 + \text{US\$ } 0.90 + \text{US\$ } 0 + \text{US\$ } 2.95 + \text{US\$ } 0.55 = \text{US\$ } 6.02 \text{ kg}^{-1}$$

- $\text{COST}_{\text{P}}$  = Biomass collection cost (US\$ 0.9; the biochar collection cost was calculated based on an unskilled labor cost of ~600 IN₹ or US\$ 7.21 for 8 h) + transportation cost (US\$ 0.72) = US\$ 1.62 kg<sup>−1</sup>
- $\text{COST}_{\text{Pro}}$  = Precursor size reduction cost (US\$ 0.9, calculated based on an unskilled labor charge of ~600 IN₹ or US\$ 7.21 for 8 h) + drying cost (US\$ 0 as it was sun-dried) = US\$ 0.9 kg<sup>−1</sup>
- $\text{COST}_{\text{A/M}}$  = US\$ 0 kg<sup>−1</sup> (as there was no activation/modification step)
- $\text{COST}_{\text{Py}}$  = Pyrolysis cost (total furnace running time × power consumption per hour × tariff rate) (US\$ 0.92) + biochar size reduction cost (based on an unskilled labor cost of ~600 IN₹ or US\$ 7.21 for 8 h (US\$ 0.9) + washing cost (US\$ 0.36, based on the consumption of water and the electricity tariff) + drying cost (US\$ 0.77, based on electricity consumption and the tariff) = US\$ 2.95 kg<sup>−1</sup>
- $\text{COST}_{\text{OTHER}}$  = 10% offset (including any mass lost during the entire process and waste disposal) = US\$ 0.55 kg<sup>−1</sup>

Large-scale production can further lower the overall NGBC700 cost because it utilizes waste as a precursor and works on affordable production techniques [68,75,76]. In this study, we estimated US\$ 6.02 kg<sup>−1</sup> of the NGBC700 to be the total preparation cost, which is lower than commercial activated carbons (US\$ 20–22 kg<sup>−1</sup>) [68].

#### 5. Conclusions

This study demonstrates that Napier grass, which produces high biomass yields, can be used to make an economical, efficient, and environmentally benign adsorption material. NGBC700 was prepared using a muffle furnace after pyrolyzing Napier grass at 700 °C (heating rate = 10 °C min<sup>−1</sup>) under limited oxygen conditions for 1 h. The NGBC700 had carbon, oxygen, and nitrogen contents of 62.8%, 30.5%, and 4.2%, respectively. SEM images confirmed the porous nature of the NGBC700, which was further supported by the BET surface area (108 m<sup>2</sup> g<sup>−1</sup>). Surface functional groups including −OH, aromatic C=C, and C-O/C-O-C were present on the NGBC700 surface and assisted in AO7 sorption. AO7 sorption decreases with an increasing pH. All sorption studies were performed at ~6.5 pH. The equilibrium time for AO7 sorption on NGBC700 was approximately 10–12 h. The PSO equation ( $R^2 = 0.964\text{--}0.997$ ) was better fitted to the kinetic data vs. the PFO equation ( $R^2 = 0.789\text{--}0.988$ ). The Freundlich isotherm ( $R^2 = 0.965$  to  $0.994$ ) was better fitted the sorption equilibrium data than the Langmuir isotherm ( $R^2 = 0.788$  to  $0.987$ ), implying AO7 sorption on heterogeneous NGBC700. The Langmuir monolayer AO7 adsorption capacity values on the NGBC700 were 14.3, 12.7, and 8.4 mg g<sup>−1</sup> at 10, 25, and 40 °C, respectively, suggesting an exothermic nature of sorption. The best AO7 desorption was achieved for three adsorption–desorption cycles by NaOH. The column AO7 sorption capacity was 4.4 mg g<sup>−1</sup>. Thomas and Yoon–Nelson column models were moderately fitted ( $R^2 = 0.76$ ) for continuous AO7 sorption on the NGBC700. The approximate production cost of NGBC700 was around US\$ 6.02 kg<sup>−1</sup>, indicating it as an economical adsorbent. In AO7-spiked (25 mg L<sup>−1</sup>) dye wastewaters obtained from local dyers, AO7 was completely removed using the NGBC700 (3 g L<sup>−1</sup>). Electrostatic interactions along with H-bonding and  $\pi\text{--}\pi$  interactions were responsible for AO7 sorption on NGBC700. Thus, low-cost NGBC700 can potentially be used for decontaminating toxic azo dyes from aqueous media. Hence, it emerges as a sustainable treatment alternative for decontamination of dye wastewater.

**Supplementary Materials:** The following supporting information can be downloaded at: <https://www.mdpi.com/article/10.3390/pr12061115/s1>, Table S1. Instruments used for NGBC700 characterization. Table S2. Local dye wastewater physicochemical parameters before and after NGBC700 treatment. Table S3. Cost estimation of NGBC700 preparation. Figure S1. Column study (A) schematic column representation, (B) actual picture of the column setup, and (C) an ideal breakthrough curve. Figure S2. NGBC700's pH<sub>pzc</sub> determination.

**Author Contributions:** Conceptualization, A.K.Y. and D.M.; methodology, A.K.Y., A.K.C. and D.M.; software, A.K.Y. and A.K.C.; validation, A.K.Y., A.K.C., T.P., S.K., B.P., V.V. and D.M.; formal analysis, A.K.Y., A.K.C., T.P., S.K., B.P. and D.M.; investigation, A.K.Y. and A.K.C.; data curation, A.K.Y.; writing—original draft preparation, A.K.Y., A.K.C., T.P., S.K., B.P., V.V. and D.M.; writing—review and editing, A.K.Y., A.K.C., T.P., S.K., B.P., V.V. and D.M.; supervision, A.K.C. and D.M.; project administration, D.M.; funding acquisition, D.M. All authors have read and agreed to the published version of the manuscript.

**Funding:** D.M. is thankful to the Principal Scientific Adviser (PSA), Government of India, for financial assistance as part of the project “Delhi Cluster-Delhi Research Implementation and Innovation” (DRIIV).

**Data Availability Statement:** The data presented in this study are available upon request from the corresponding author.

**Acknowledgments:** The authors acknowledge the Central Instrumentation Facilities (CIF) at the School of Physical Sciences (SPS), Jawaharlal Nehru University, New Delhi, for BET surface area measurement, and the Advanced Instrumentation Research Facility (AIRF) at Jawaharlal Nehru University, New Delhi, for providing access to SEM, SEM-EDX, and TEM facilities. One of the authors (AKY) would like to thank Pratima R Solanki, Special Centre for Nanoscience (SCNS) at Jawaharlal Nehru University, New Delhi, for giving access to the FTIR and XRD facilities.

**Conflicts of Interest:** The authors declare no conflicts of interest.

## References

1. Khan, W.U.; Ahmed, S.; Dhoble, Y.; Madhav, S. A critical review of hazardous waste generation from textile industries and associated ecological impacts. *J. Indian Chem. Soc.* **2023**, *100*, 100829. [[CrossRef](#)]
2. Al-Tohamy, R.; Ali, S.S.; Li, F.; Okasha, K.M.; Mahmoud, Y.A.; Elsamahy, T.; Jiao, H.; Fu, Y.; Sun, J. A critical review on the treatment of dye-containing wastewater: Ecotoxicological and health concerns of textile dyes and possible remediation approaches for environmental safety. *Ecotoxicol. Environ. Saf.* **2022**, *231*, 113160. [[CrossRef](#)] [[PubMed](#)]
3. Kaur, A.; Taylor, K.E.; Biswas, N. Soybean peroxidase-catalyzed degradation of a sulfonated dye and its azo-cleavage product. *J. Chem. Technol. Biotechnol.* **2021**, *96*, 423–430. [[CrossRef](#)]
4. Lellis, B.; Fávaro-Polonio, C.Z.; Pamphile, J.A.; Polonio, J.C. Effects of textile dyes on health and the environment and bioremediation potential of living organisms. *Biotechnol. Res. Innov.* **2019**, *3*, 275–290. [[CrossRef](#)]
5. Alsukaibi, A.K.D. Various Approaches for the Detoxification of Toxic Dyes in Wastewater. *Processes* **2022**, *10*, 1968. [[CrossRef](#)]
6. Adegoke, K.A.; Bello, O.S. Dye sequestration using agricultural wastes as adsorbents. *Water Resour. Ind.* **2015**, *12*, 8–24. [[CrossRef](#)]
7. Esmaeili, S.; Ashrafi-Kooshk, M.R.; Khaledian, K.; Adibi, H.; Rouhani, S.; Khodarahmi, R. Degradation products of the artificial azo dye, Allura red, inhibit esterase activity of carbonic anhydrase II: A basic in vitro study on the food safety of the colorant in terms of enzyme inhibition. *Food Chem.* **2016**, *213*, 494–504. [[CrossRef](#)] [[PubMed](#)]
8. Samsami, S.; Mohamadi, M.; Sarrafzadeh, M.H.; Rene, E.R.; Firoozbahr, M. Recent advances in the treatment of dye-containing wastewater from textile industries: Overview and perspectives. *Process Saf. Environ. Prot.* **2020**, *143*, 138–163. [[CrossRef](#)]
9. Yaseen, D.A.; Scholz, M. Textile dye wastewater characteristics and constituents of synthetic effluents: A critical review. *Int. J. Environ. Sci. Technol.* **2018**, *16*, 1193–1226. [[CrossRef](#)]
10. Jegatheesan, V.; Pramanik, B.K.; Chen, J.; Navaratna, D.; Chang, C.Y.; Shu, L. Treatment of textile wastewater with membrane bioreactor: A critical review. *Bioresour. Technol.* **2016**, *204*, 202–212. [[CrossRef](#)]
11. Ahmadian, M.; Derakhshankhah, H.; Jaymand, M. Biosorptive removal of organic dyes using natural gums-based materials: A comprehensive review. *J. Ind. Eng. Chem.* **2023**, *124*, 102–131. [[CrossRef](#)]
12. Srivastava, P.; Al-Obaidi, S.A.; Webster, G.; Weightman, A.J.; Sapsford, D.J. Towards passive bioremediation of dye-bearing effluents using hydrous ferric oxide wastes: Mechanisms, products and microbiology. *J. Environ. Manag.* **2022**, *317*, 115332. [[CrossRef](#)] [[PubMed](#)]
13. Benkhaya, S.; Mrabet, S.; El Harfi, A. A review on classifications, recent synthesis and applications of textile dyes. *Inorg. Chem. Commun.* **2020**, *115*, 107891. [[CrossRef](#)]
14. Chequer, F.D.; De Oliveira, G.R.; Ferraz, E.A.; Cardoso, J.C.; Zanoni, M.B.; de Oliveira, D.P. Textile Dyes: Dyeing Process and Environmental Impact. In *Eco-Friendly Textile Dyeing and Finishing*; Günay, M., Ed.; IntechOpen: Rijeka, Croatia, 2013; pp. 151–176.

15. Eleryan, A.; Hassaan, M.A.; Aigbe, U.O.; Ukhurebor, K.E.; Onyancha, R.B.; El-Nemr, M.A.; Ragab, S.; Hossain, I.; El Nemr, A. Kinetic and isotherm studies of Acid Orange 7 dye absorption using sulphonated mandarin biochar treated with TETA. *Biomass Convers. Biorefinery* **2023**, *14*, 10599–10610. [\[CrossRef\]](#)
16. Sabnis, R.W. *Handbook of Biological Dyes and Stains: Synthesis and Industrial Applications*; John Wiley & Sons: Hoboken, NJ, USA, 2010; p. 521.
17. Perera, H.J. Removal of Acid Orange 7 Dye from Wastewater: Review. *Int. J. Waste Resour.* **2019**, *9*, 1–4. [\[CrossRef\]](#)
18. Gupta, V.K.; Mittal, A.; Gajbe, V.; Mittal, J. Removal and Recovery of the Hazardous Azo Dye Acid Orange 7 through Adsorption over Waste Materials: Bottom Ash and De-Oiled Soya. *Ind. Eng. Chem. Res.* **2006**, *45*, 1446–1453. [\[CrossRef\]](#)
19. Nunes, M.J.; Lopes, A.; Pacheco, M.J.; Ciriaco, L. Visible-Light-Driven AO7 Photocatalytic Degradation and Toxicity Removal at Bi-Doped SrTiO(3). *Materials* **2022**, *15*, 2465. [\[CrossRef\]](#)
20. Tong, W.S.; Oo, C.W.; Sudesh, K.; Ng, S.L. Decolorization of acid orange 7 in moving bed biofilm reactor packed with polyhydroxalkanoate/activated carbon. *J. Water Process Eng.* **2024**, *58*, 104750. [\[CrossRef\]](#)
21. Gasmi, I.; Kerboua, K.; Haddour, N.; Hamdaoui, O.; Alghyamah, A.; Buret, F. The Galvano-Fenton process: Experimental insights and numerical mechanistic investigation applied to the degradation of acid orange 7. *Electrochim. Acta* **2021**, *373*, 137897. [\[CrossRef\]](#)
22. Mancuso, A.; Sacco, O.; Sannino, D.; Pragliola, S.; Vaiano, V. Enhanced visible-light-driven photodegradation of Acid Orange 7 azo dye in aqueous solution using Fe-N co-doped TiO<sub>2</sub>. *Arab. J. Chem.* **2020**, *13*, 8347–8360. [\[CrossRef\]](#)
23. Han, F.; Kambala, V.S.R.; Dharmarajan, R.; Liu, Y.; Naidu, R. Photocatalytic degradation of azo dye acid orange 7 using different light sources over Fe<sup>3+</sup>-doped TiO<sub>2</sub> nanocatalysts. *Environ. Technol. Innov.* **2018**, *12*, 27–42. [\[CrossRef\]](#)
24. Xia, Y.; Wang, G.; Guo, L.; Dai, Q.; Ma, X. Electrochemical oxidation of Acid Orange 7 azo dye using a PbO<sub>2</sub> electrode: Parameter optimization, reaction mechanism and toxicity evaluation. *Chemosphere* **2020**, *241*, 125010. [\[CrossRef\]](#) [\[PubMed\]](#)
25. Qiao, Q.; Singh, S.; Lo, S.-L.; Li, Y.; Jin, J.; Wang, L. Electrochemical oxidation of acid orange 7 dye with Ce, Nd, and Co-modified PbO<sub>2</sub> electrodes: Preparation, characterization, optimization, and mineralization. *J. Taiwan Inst. Chem. Eng.* **2018**, *84*, 110–122. [\[CrossRef\]](#)
26. Cojocaru, C.; Clima, L. Polymer assisted ultrafiltration of AO7 anionic dye from aqueous solutions: Experimental design, multivariate optimization, and molecular docking insights. *J. Membr. Sci.* **2020**, *604*, 118054. [\[CrossRef\]](#)
27. Xu, Y.; Lebrun, R.E.; Gallo, P.-J.; Blond, P. Treatment of Textile Dye Plant Effluent by Nanofiltration Membrane. *Sep. Sci. Technol.* **1999**, *34*, 2501–2519. [\[CrossRef\]](#)
28. Lau, Y.Y.; Wong, Y.S.; Teng, T.T.; Morad, N.; Rafatullah, M.; Ong, S.A. Coagulation-flocculation of azo dye acid orange 7 with green refined laterite soil. *Chem. Eng. J.* **2014**, *246*, 383–390. [\[CrossRef\]](#)
29. Sharma, M.; Sharma, S.; Akhtar, M.S.; Kumar, R.; Umar, A.; Alkhanjaf, A.A.M.; Baskoutas, S. Microorganisms-assisted degradation of Acid Orange 7 dye: A review. *Int. J. Environ. Sci. Technol.* **2024**, *21*, 6133–6166. [\[CrossRef\]](#)
30. Cojocaru, C.; Samoila, P.; Pascariu, P. Chitosan-based magnetic adsorbent for removal of water-soluble anionic dye: Artificial neural network modeling and molecular docking insights. *Int. J. Biol. Macromol.* **2019**, *123*, 587–599. [\[CrossRef\]](#)
31. Yardımcı, B.; Kanmaz, N.; Buğdaycı, M.; Demirci, P. Synthesis of CuBDC metal-organic framework supported zinc oxide via ball-milling technique for enhanced adsorption of Orange-II. *Surf. Interfaces* **2024**, *46*, 104122. [\[CrossRef\]](#)
32. Lei, Y.; Zhao, J.; Song, H.; Yang, F.; Shen, L.; Zhu, L.; Zeng, Z.; Li, X.; Wang, G. Enhanced adsorption of dyes by functionalized UiO-66 nanoparticles: Adsorption properties and mechanisms. *J. Mol. Struct.* **2023**, *1292*, 136111. [\[CrossRef\]](#)
33. Mohan, D.; Chaubey, A.K.; Patel, M.; Navarathna, C.; Mlsna, T.E.; Pittman, C.U., Jr. Biochar adsorption system designs. In *Sustainable Biochar for Water and Wastewater Treatment*; Mohan, D., Pittman, C.U., Jr., Mlsna, T.E., Eds.; Elsevier: Amsterdam, The Netherlands, 2022; pp. 153–203.
34. Khalil, A.; Mangwandi, C.; Salem, M.A.; Ragab, S.; El Nemr, A. Orange peel magnetic activated carbon for removal of acid orange 7 dye from water. *Sci. Rep.* **2024**, *14*, 119. [\[CrossRef\]](#) [\[PubMed\]](#)
35. Li, J.; Lin, H.; Zhu, K.; Zhang, H. Degradation of Acid Orange 7 using peroxymonosulfate catalyzed by granulated activated carbon and enhanced by electrolysis. *Chemosphere* **2017**, *188*, 139–147. [\[CrossRef\]](#) [\[PubMed\]](#)
36. Bourahla, S.; Nemchi, F.; Belayachi, H.; Belayachi, A.; Harrats, C.; Belhakem, M. Removal of the AO7 dye by adsorption on activated carbon based on grape marc: Equilibrium, regeneration, and FTIR spectroscopy. *J. Iran. Chem. Soc.* **2023**, *20*, 669–681. [\[CrossRef\]](#)
37. Yoon, S.; Calvo, J.J.; So, M.C. Removal of Acid Orange 7 from Aqueous Solution by Metal-Organic Frameworks. *Crystals* **2019**, *9*, 17. [\[CrossRef\]](#)
38. Hajjaji, W.; Pullar, R.C.; Labrincha, J.A.; Rocha, F. Aqueous Acid Orange 7 dye removal by clay and red mud mixes. *Appl. Clay Sci.* **2016**, *126*, 197–206. [\[CrossRef\]](#)
39. Naraghi, B.; Zabihi, F.; Narooie, M.R.; Saeidi, M.; Biglari, H. Removal of Acid Orange 7 dye from aqueous solutions by adsorption onto Kenya tea pulps; granulated shape. *Electron. Physician* **2017**, *9*, 4312–4321. [\[CrossRef\]](#) [\[PubMed\]](#)
40. Gogoi, N.; Samanta, P.; Dahutia, P. Agro-Wastes as Low-Cost Biosorbent for Dyes Removal from Wastewater. In *Agriculture Waste Management and Bioresource*; John Wiley & Sons: Hoboken, NJ, USA, 2023; pp. 149–172.
41. Deokar, S.; Patel, H.; Thakare, P.; Bhagat, S.; Gedam, V.; Pathak, P. Adsorptive column studies for removal of acid orange 7 dye using bagasse fly ash. *Indian J. Chem. Technol.* **2021**, *28*, 319–327.



42. Khosla, E.; Kaur, S.; Dave, P.N. Mechanistic Study of Adsorption of Acid Orange-7 over Aluminum Oxide Nanoparticles. *J. Eng.* **2013**, *2013*, 593534. [\[CrossRef\]](#)
43. Yen Doan, T.H.; Van Dang, L.; Trang Truong, T.T.; Vu, T.N.; Le, T.S.; Thu Nguyen, T.M.; Nguyen, M.N.; Pham, T.T.; Yusa, S.-i.; Pham, T.D. Removal of Acid Orange G Azo Dye by Polycation-Modified Alpha Alumina Nanoparticles. *Chem. Asian J.* **2023**, *18*, e202300404. [\[CrossRef\]](#) [\[PubMed\]](#)
44. Perez-Calderon, J.; Marin-Silva, D.A.; Zaritzky, N.; Pinotti, A. Eco-friendly PVA-chitosan adsorbent films for the removal of azo dye Acid Orange 7: Physical cross-linking, adsorption process, and reuse of the material. *Adv. Ind. Eng. Polym. Res.* **2023**, *6*, 239–254. [\[CrossRef\]](#)
45. Marovska, G.; Dushkova, M.; Angelova, G.; Brazkova, M.; Brink, H.; Haneklaus, N.; Menkov, N.; Slavov, A. Rose and lavender industrial by-products application for adsorption of Acid Orange 7 from aqueous solution. *Biomass Convers. Biorefinery* **2023**, 1–14. [\[CrossRef\]](#)
46. Dong, S.; Zheng, Q.; Huang, G.; Wang, X.; Huang, T. The Coordination Polymer [Cu(bipy)(SO<sub>4</sub>)]<sub>n</sub> and Its Functionalization for Selective Removal of Two Types of Organic Pollutants. *Ind. Eng. Chem. Res.* **2019**, *58*, 15416–15424. [\[CrossRef\]](#)
47. Ahmadian, A.; Goharrizi, B.A.; Shahriari, T.; Ahmadi, S. Adsorption of chromium (VI) and Acid Orange 7 on lemon peel biochar: A response surface methodology approach. *Int. J. Environ. Sci. Technol.* **2023**, *20*, 2939–2958. [\[CrossRef\]](#)
48. Zhang, M.; Lin, K.; Zhong, Y.; Zhang, D.; Ahmad, M.; Yu, J.; Fu, H.; Xu, L.; Wu, S.; Huang, L. Functionalizing biochar by Co-pyrolysis shaddock peel with red mud for removing acid orange 7 from water. *Environ. Pollut.* **2022**, *299*, 118893. [\[CrossRef\]](#) [\[PubMed\]](#)
49. Kapoor, R.T.; Sivamani, S. Biosorption behavior of acid orange 7 dye onto Cucumis sativus peel biochar and its effect on growth of Triticum aestivum. *Environ. Prog. Sustain. Energy* **2023**, *42*, e14106. [\[CrossRef\]](#)
50. Patel, M.; Kumar, R.; Pittman, C.U., Jr.; Mohan, D. Ciprofloxacin and acetaminophen sorption onto banana peel biochars: Environmental and process parameter influences. *Environ. Res.* **2021**, *201*, 111218. [\[CrossRef\]](#) [\[PubMed\]](#)
51. Mohan, D.; Sarswat, A.; Ok, Y.S.; Pittman, C.U., Jr. Organic and inorganic contaminants removal from water with biochar, a renewable, low cost and sustainable adsorbent—A critical review. *Bioresour. Technol.* **2014**, *160*, 191–202. [\[CrossRef\]](#) [\[PubMed\]](#)
52. Patel, M.; Kumar, R.; Kishor, K.; Mlsna, T.; Pittman, C.U., Jr.; Mohan, D. Pharmaceuticals of Emerging Concern in Aquatic Systems: Chemistry, Occurrence, Effects, and Removal Methods. *Chem. Rev.* **2019**, *119*, 3510–3673. [\[CrossRef\]](#) [\[PubMed\]](#)
53. Amalina, F.; Razak, A.S.A.; Krishnan, S.; Zularisam, A.W.; Nasrullah, M. A comprehensive assessment of the method for producing biochar, its characterization, stability, and potential applications in regenerative economic sustainability—A review. *Clean. Mater.* **2022**, *3*, 100045. [\[CrossRef\]](#)
54. Dissanayake, P.D.; Choi, S.W.; Igalavithana, A.D.; Yang, X.; Tsang, D.C.W.; Wang, C.-H.; Kua, H.W.; Lee, K.B.; Ok, Y.S. Sustainable gasification biochar as a high efficiency adsorbent for CO<sub>2</sub> capture: A facile method to designer biochar fabrication. *Renew. Sustain. Energy Rev.* **2020**, *124*, 109785. [\[CrossRef\]](#)
55. Tongpoothorn, W.; Somboon, T.; Sriuttha, M. The Utilization of Napier Grass Stems for Cd(II) Ions Removal from Aqueous Solution: Process Optimization Studies Using Response Surface Methodology. *Naresuan Univ. J. Sci. Technol.* **2020**, *28*, 46–62.
56. Reza, M.S.; Afroze, S.; Bakar, M.S.A.; Saidur, R.; Aslfattahi, N.; Taweekun, J.; Azad, A.K. Biochar characterization of invasive Pennisetum purpureum grass: Effect of pyrolysis temperature. *Biochar* **2020**, *2*, 239–251. [\[CrossRef\]](#)
57. Mustapha, O.R.; Osobamiro, T.M.; Sanyaolu, N.O.; Alabi, O.M. Adsorption study of Methylene blue dye: An effluents from local textile industry using Pennistum pupureum (elephant grass). *Int. J. Phytorem.* **2023**, *25*, 1348–1358. [\[CrossRef\]](#) [\[PubMed\]](#)
58. Grey, T.L.; Webster, T.M.; Li, X.; Anderson, W.; Cutts, G.S. Evaluation of Control of Napiergrass (*Pennisetum purpureum*) with Tillage and Herbicides. *Invasive Plant Sci. Manag.* **2015**, *8*, 393–400, 398. [\[CrossRef\]](#)
59. Ferreira, S.D.; Lazzarotto, I.P.; Junges, J.; Manera, C.; Godinho, M.; Osório, E. Steam gasification of biochar derived from elephant grass pyrolysis in a screw reactor. *Energy Convers. Manag.* **2017**, *153*, 163–174. [\[CrossRef\]](#)
60. Essandoh, M.; Kunwar, B.; Pittman, C.U., Jr.; Mohan, D.; Mlsna, T. Sorptive removal of salicylic acid and ibuprofen from aqueous solutions using pine wood fast pyrolysis biochar. *Chem. Eng. J.* **2015**, *265*, 219–227. [\[CrossRef\]](#)
61. D1762-84; Standard Test Method for Chemical Analysis of Wood Charcoal. ASTM: West Conshohocken, PA, USA, 2021.
62. Lagergren, S. Zur theorie der sogenannten adsorption geloster stoffe. *K. Sven. Vetenskapsakademiens. Handl.* **1898**, *24*, 1–39.
63. Ho, Y.S.; McKay, G. Pseudo-second order model for sorption processes. *Process Biochem.* **1999**, *34*, 451–465. [\[CrossRef\]](#)
64. Langmuir, I. The adsorption of gases on plane surfaces of glass, mica and platinum. *J. Am. Chem. Soc.* **1918**, *40*, 1361–1403. [\[CrossRef\]](#)
65. Freundlich, H. Over the adsorption in solution. *J. Phys. Chem.* **1906**, *57*, 1100–1107.
66. Choudhary, V.; Patel, M.; Pittman, C.U., Jr.; Mohan, D. Batch and Continuous Fixed-Bed Lead Removal Using Himalayan Pine Needle Biochar: Isotherm and Kinetic Studies. *ACS Omega* **2020**, *5*, 16366–16378. [\[CrossRef\]](#) [\[PubMed\]](#)
67. Chaubey, A.K.; Patel, M.; Pittman, C.U., Jr.; Mohan, D. Acetaminophen and trimethoprim batch and fixed-bed sorption on MgO/Al<sub>2</sub>O<sub>3</sub>-modified rice husk biochar. *Colloids Surf. A Physicochem. Eng. Asp.* **2023**, *677*, 132263. [\[CrossRef\]](#)
68. Patel, M.; Chaubey, A.K.; Pittman, C.U., Jr.; Mohan, D. Aqueous ibuprofen sorption by using activated walnut shell biochar: Process optimization and cost estimation. *Environ. Sci. Adv.* **2022**, *1*, 530–545. [\[CrossRef\]](#)
69. Manjunath, S.V.; Kumar, M. Simultaneous removal of antibiotic and nutrients via Prosopis juliflora activated carbon column: Performance evaluation, effect of operational parameters and breakthrough modeling. *Chemosphere* **2021**, *262*, 127820. [\[CrossRef\]](#)

70. Chatterjee, A.; Schiewer, S. Biosorption of Cadmium(II) Ions by Citrus Peels in a Packed Bed Column: Effect of Process Parameters and Comparison of Different Breakthrough Curve Models. *CLEAN Soil Air Water* **2011**, *39*, 874–881. [\[CrossRef\]](#)
71. Tran, T.C.P.; Nguyen, T.P.; Nguyen, X.C.; Nguyen, X.H.; Nguyen, T.A.H.; Nguyen, T.T.N.; Vo, T.Y.B.; Nguyen, T.H.G.; Nguyen, T.T.H.; Vo, T.D.H.; et al. Adsorptive removal of phosphate from aqueous solutions using low-cost modified biochar-packed column: Effect of operational parameters and kinetic study. *Chemosphere* **2022**, *309*, 136628. [\[CrossRef\]](#) [\[PubMed\]](#)
72. Thomas, H.C. Heterogeneous ion exchange in a flowing system. *J. Am. Chem. Soc.* **1944**, *66*, 1664–1666. [\[CrossRef\]](#)
73. Chu, K.H. Fixed bed sorption: Setting the record straight on the Bohart–Adams and Thomas models. *J. Hazard. Mater.* **2010**, *177*, 1006–1012. [\[CrossRef\]](#) [\[PubMed\]](#)
74. Yoon, Y.H.; Nelson, J.H. Application of Gas Adsorption Kinetics I. A Theoretical Model for Respirator Cartridge Service Life. *Am. Ind. Hyg. Assoc. J.* **1984**, *45*, 509–516. [\[CrossRef\]](#) [\[PubMed\]](#)
75. Chakraborty, P.; Banerjee, S.; Kumar, S.; Sadhukhan, S.; Halder, G. Elucidation of ibuprofen uptake capability of raw and steam activated biochar of Aegle marmelos shell: Isotherm, kinetics, thermodynamics and cost estimation. *Process Saf. Environ. Prot.* **2018**, *118*, 10–23. [\[CrossRef\]](#)
76. Chakraborty, P.; Show, S.; Banerjee, S.; Halder, G. Mechanistic insight into sorptive elimination of ibuprofen employing bi-directional activated biochar from sugarcane bagasse: Performance evaluation and cost estimation. *J. Environ. Chem. Eng.* **2018**, *6*, 5287–5300. [\[CrossRef\]](#)
77. Claoston, N.; Samsuri, A.W.; Ahmad Husni, M.H.; Mohd Amran, M.S. Effects of pyrolysis temperature on the physicochemical properties of empty fruit bunch and rice husk biochars. *Waste Manag. Res.* **2014**, *32*, 331–339. [\[CrossRef\]](#) [\[PubMed\]](#)
78. Johnston, C.T. Biochar analysis by Fourier-transform infra-red spectroscopy. In *Biochar: A Guide to Analytical Methods*; Balwant Singh, M.C.-A., Lehmann, J., Eds.; CSIRO Publishing: Clayton, Australia, 2017; pp. 199–213.
79. Lafuente, B.; Downs, R.T.; Yang, H.; Stone, N. The power of databases: The RRUFF project. In *Highlights in Mineralogical Crystallography*; Armbruster, T., Danisi, R.M., Eds.; De Gruyter (O): Berlin, Germany, 2016; pp. 1–30.
80. Zhao, H.; Lang, Y. Adsorption behaviors and mechanisms of florfenicol by magnetic functionalized biochar and reed biochar. *J. Taiwan Inst. Chem. Eng.* **2018**, *88*, 152–160. [\[CrossRef\]](#)
81. Stuart, B.H. *Infrared Spectroscopy: Fundamentals and Applications*; John Wiley & Sons Ltd.: Chichester, UK, 2004; p. 248.
82. Lyu, H.; Gao, B.; He, F.; Zimmerman, A.R.; Ding, C.; Huang, H.; Tang, J. Effects of ball milling on the physicochemical and sorptive properties of biochar: Experimental observations and governing mechanisms. *Environ. Pollut.* **2018**, *233*, 54–63. [\[CrossRef\]](#) [\[PubMed\]](#)
83. Mohan, D.; Singh, P.; Sarswat, A.; Steele, P.H.; Pittman, C.U., Jr. Lead sorptive removal using magnetic and nonmagnetic fast pyrolysis energy cane biochars. *J. Colloid Interface Sci.* **2015**, *448*, 238–250. [\[CrossRef\]](#) [\[PubMed\]](#)
84. Vimal, V.; Patel, M.; Mohan, D. Aqueous carbofuran removal using slow pyrolyzed sugarcane bagasse biochar: Equilibrium and fixed-bed studies. *RSC Adv.* **2019**, *9*, 26338–26350. [\[CrossRef\]](#) [\[PubMed\]](#)
85. Mohan, D.; Abhishek, K.; Sarswat, A.; Patel, M.; Singh, P.; Pittman, C.U., Jr. Biochar production and applications in soil fertility and carbon sequestration—A sustainable solution to crop-residue burning in India. *RSC Adv.* **2018**, *8*, 508–520. [\[CrossRef\]](#)
86. Chia, C.H.; Gong, B.; Joseph, S.D.; Marjo, C.E.; Munroe, P.; Rich, A.M. Imaging of mineral-enriched biochar by FTIR, Raman and SEM–EDX. *Vib. Spectrosc.* **2012**, *62*, 248–257. [\[CrossRef\]](#)
87. Singh, B.; Raven, M.D. X-ray diffraction analysis of biochar. In *Biochar: A Guide to Analytical Methods*; Singh, B., Camps-Arbestain, M., Lehmann, J., Eds.; CSIRO Publishing: Clayton, Australia, 2017; pp. 245–252.
88. Downs, R.T.; Hall-Wallace, M. The American Mineralogist crystal structure database. *Am. Mineral.* **2003**, *88*, 247–250.
89. Peng, H.; Li, K.; Wang, T.; Wang, J.; Wang, J.; Zhu, R.; Sun, D.; Wang, S. Preparation of hierarchical mesoporous CaCO<sub>3</sub> by a facile binary solvent approach as anticancer drug carrier for etoposide. *Nanoscale Res. Lett.* **2013**, *8*, 321. [\[CrossRef\]](#)
90. Wang, J.; Liao, Z.; Ifthikar, J.; Shi, L.; Chen, Z.; Chen, Z. One-step preparation and application of magnetic sludge-derived biochar on acid orange 7 removal via both adsorption and persulfate based oxidation. *RSC Adv.* **2017**, *7*, 18696–18706. [\[CrossRef\]](#)
91. Stoyanova, M.; Slavova, I.; Christoskova, S.; Ivanova, V. Catalytic performance of supported nanosized cobalt and iron–cobalt mixed oxides on MgO in oxidative degradation of Acid Orange 7 azo dye with peroxymonosulfate. *Appl. Catal. A Gen.* **2014**, *476*, 121–132. [\[CrossRef\]](#)
92. El-Nemr, M.; Abdelmonem, N.; Ismail, I.; Ragab, S.; El Nemr, A. The efficient removal of the hazardous azo dye Acid Orange 7 from water using modified biochar from Pea-peels. *Desalination Water Treat.* **2020**, *203*, 327–355. [\[CrossRef\]](#)
93. Ghaly, A.; Ananthashankar, R.; Alhattab, M.; Ramakrishnan, V.V. Production, characterization and treatment of textile effluents: A critical review. *J. Chem. Eng. Process. Technol.* **2014**, *5*, 1–19.
94. Rauf, M.A.; Ashraf, S.S. Fundamental principles and application of heterogeneous photocatalytic degradation of dyes in solution. *Chem. Eng. J.* **2009**, *151*, 10–18. [\[CrossRef\]](#)
95. Styliadi, M.; Kondarides, D.I.; Verykios, X.E. Pathways of solar light-induced photocatalytic degradation of azo dyes in aqueous TiO<sub>2</sub> suspensions. *Appl. Catal. B Environ.* **2003**, *40*, 271–286. [\[CrossRef\]](#)
96. Lin, R.; Liang, Z.; Yang, C.; Zhao, Z.; Cui, F. Selective adsorption of organic pigments on inorganically modified mesoporous biochar and its mechanism based on molecular structure. *J. Colloid Interface Sci.* **2020**, *573*, 21–30. [\[CrossRef\]](#) [\[PubMed\]](#)
97. Jung, K.-W.; Choi, B.H.; Hwang, M.-J.; Jeong, T.-U.; Ahn, K.-H. Fabrication of granular activated carbons derived from spent coffee grounds by entrapment in calcium alginate beads for adsorption of acid orange 7 and methylene blue. *Bioresour. Technol.* **2016**, *219*, 185–195. [\[CrossRef\]](#) [\[PubMed\]](#)

98. Qiu, Y.; Xu, X.; Xu, Z.; Liang, J.; Yu, Y.; Cao, X. Contribution of different iron species in the iron-biochar composites to sorption and degradation of two dyes with varying properties. *Chem. Eng. J.* **2020**, *389*, 124471. [[CrossRef](#)]
99. Sahoo, T.R.; Prelot, B. Adsorption processes for the removal of contaminants from wastewater: The perspective role of nanomaterials and nanotechnology. In *Nanomaterials for the Detection and Removal of Wastewater Pollutants*; Bonelli, B., Freyria, F.S., Rossetti, I., Sethi, R., Eds.; Elsevier: Amsterdam, The Netherlands, 2020; pp. 161–222.
100. Lian, F.; Cui, G.; Liu, Z.; Duo, L.; Zhang, G.; Xing, B. One-step synthesis of a novel N-doped microporous biochar derived from crop straws with high dye adsorption capacity. *J. Environ. Manag.* **2016**, *176*, 61–68. [[CrossRef](#)] [[PubMed](#)]
101. Foo, K.Y.; Hameed, B.H. Insights into the modeling of adsorption isotherm systems. *Chem. Eng. J.* **2010**, *156*, 2–10. [[CrossRef](#)]
102. Mu, Y.; Ma, H. NaOH-modified mesoporous biochar derived from tea residue for methylene Blue and Orange II removal. *Chem. Eng. Res. Des.* **2021**, *167*, 129–140. [[CrossRef](#)]
103. Thirunavukkarasu, A.; Nithya, R. Adsorption of acid orange 7 using green synthesized CaO/CeO<sub>2</sub> composite: An insight into kinetics, equilibrium, thermodynamics, mass transfer and statistical models. *J. Taiwan Inst. Chem. Eng.* **2020**, *111*, 44–62. [[CrossRef](#)]
104. Chen, S.; Qin, C.; Wang, T.; Chen, F.; Li, X.; Hou, H.; Zhou, M. Study on the adsorption of dyestuffs with different properties by sludge-rice husk biochar: Adsorption capacity, isotherm, kinetic, thermodynamics and mechanism. *J. Mol. Liq.* **2019**, *285*, 62–74. [[CrossRef](#)]
105. Ghasemi, A.; Shams, M.; Qasemi, M.; Afsharnia, M. Data on efficient removal of acid orange 7 by zeolitic imidazolate framework-8. *Data Brief* **2019**, *23*, 103783. [[CrossRef](#)] [[PubMed](#)]
106. Noorimotlagh, Z.; Darvishi Cheshmeh Soltani, R.; Khataee, A.R.; Shahriyar, S.; Nourmoradi, H. Adsorption of a textile dye in aqueous phase using mesoporous activated carbon prepared from Iranian milk vetch. *J. Taiwan Inst. Chem. Eng.* **2014**, *45*, 1783–1791. [[CrossRef](#)]
107. Hsiu-Mei, C.; Ting-Chien, C.; San-De, P.; Chiang, H.-L. Adsorption characteristics of Orange II and Chrysophenine on sludge adsorbent and activated carbon fibers. *J. Hazard. Mater.* **2009**, *161*, 1384–1390. [[CrossRef](#)] [[PubMed](#)]
108. Jia, L.; Liu, W.; Cao, J.; Wu, Z.; Yang, C. Modified multi-walled carbon nanotubes assisted foam fractionation for effective removal of acid orange 7 from the dyestuff wastewater. *J. Environ. Manag.* **2020**, *262*, 110260. [[CrossRef](#)] [[PubMed](#)]
109. Li, J.; Du, Y.; Deng, B.; Zhu, K.; Zhang, H. Activated carbon adsorptive removal of azo dye and peroxydisulfate regeneration: From a batch study to continuous column operation. *Environ. Sci. Pollut. Res.* **2017**, *24*, 4932–4941. [[CrossRef](#)] [[PubMed](#)]
110. Yang, Z.; Zhu, L.; Chen, L. Selective adsorption and separation of dyes from aqueous solution by core-shell structured NH<sub>2</sub>-functionalized UiO-66 magnetic composites. *J. Colloid Interface Sci.* **2019**, *539*, 76–86. [[CrossRef](#)] [[PubMed](#)]
111. Santhosh, C.; Daneshvar, E.; Tripathi, K.M.; Baltrėnas, P.; Kim, T.; Baltrėnaitė, E.; Bhatnagar, A. Synthesis and characterization of magnetic biochar adsorbents for the removal of Cr(VI) and Acid orange 7 dye from aqueous solution. *Environ. Sci. Pollut. Res.* **2020**, *27*, 32874–32887. [[CrossRef](#)] [[PubMed](#)]
112. Rajeshkanna, P.; Nagarajan, N.; Meenakshi, S. Rhodamine B and acid orange 7 adsorption onto activated carbon from deinked pulp waste sludge: Adsorption and kinetics studies. *Environ. Sci.* **2018**, *14*, 169.
113. Wathukarage, A.; Herath, I.; Iqbal, M.C.M.; Vithanage, M. Mechanistic understanding of crystal violet dye sorption by woody biochar: Implications for wastewater treatment. *Environ. Geochem. Health* **2019**, *41*, 1647–1661. [[CrossRef](#)] [[PubMed](#)]

**Disclaimer/Publisher’s Note:** The statements, opinions and data contained in all publications are solely those of the individual author(s) and contributor(s) and not of MDPI and/or the editor(s). MDPI and/or the editor(s) disclaim responsibility for any injury to people or property resulting from any ideas, methods, instructions or products referred to in the content.